Assessment of Aeroacoustic Simulations of the High-Lift Common Research Model

David P. Lockard[*], Matthew D. O'Connell[†], Veer N. Vatsa[‡], and Meelan M. Choudhari[§]

NASA Langley Research Center, Hampton,VA 23681

This paper presents further validation of PowerFLOW® aeroacoustic simulations of the High-Lift Common Research Model through comparisons with experimental data from a recently completed wind tunnel test. Preliminary time-averaged surface pressure and microphone array data from the experiment are in reasonably good agreement with the simulations, and the slat is shown to be a dominant noise source on this model. The simulations did not predict slat tones that were very prominent in the experiment, but they did capture the broadband component of slat noise in the low-frequency range up to 1 kHz at full scale. Future tests are planned to demonstrate slat noise reduction technology, and simulations are being used to guide this development.

Nomenclature

a	speed of sound		$|\mathbf{V}|$	magnitude of velocity vector
f	frequency		rms	root mean square
C_p	coefficient of pressure		VR	variable resolution
FSS	full-span slat		x, y, z	Cartesian coordinates
M	Mach number $= |\mathbf{V}|/a$			
PSD	power spectral density (dB/Hz)		**Greek:**	
PSS	part-span slat		η	normalized spanwise distance

I. Introduction

Aircraft noise reduction, including that of the airframe, is an important goal of the NASA Advanced Air Transport Technology (AATT) Project, which is supporting a combined experimental and computational effort to better understand and mitigate the sources associated with slat noise. The nonpropulsive (or airframe) sources of aircraft noise include high-lift devices (e.g., the leading-edge slat and trailing-edge flaps) and the aircraft undercarriage. The ranking of these sources is configuration dependent; however, both model-scale tests [1–7] and flyover noise measurements [8] have identified the leading-edge slat as a prominent source of airframe noise during aircraft approach. To further develop airframe noise reduction technology, NASA has constructed a 10%-scale version of the High-Lift Common Research Model (HL-CRM) developed by Lacy and Sclafani [9]. The original cruise configuration NASA CRM is an open geometry that has been widely used in the AIAA Drag Prediction Workshops [10]. The NASA CRM [11] consists of a contemporary supercritical transonic wing with flow-through nacelles and a fuselage that is representative of a widebody commercial transport aircraft. The new HL-CRM is also an open geometry that was used in the AIAA Geometry and Mesh Generation Workshop [12] and the 3rd AIAA High-Lift Prediction Workshop [13].

Two views of the HL-CRM in the NASA Langley Research Center (LaRC) 14- by 22-foot (14x22) subsonic tunnel are shown in Fig. 1. The geometry includes inboard and outboard flaps that meet in the center. There are also inboard and outboard slats, but there is a gap between them to accommodate the pylon for a flow-through nacelle. This is referred to as the part-span slat (PSS) configuration, but the nacelle/pylon can be removed and a bridge piece inserted between the slats to form a full-span slat (FSS). In the landing mode, both flap deflections are set to 37° and the slat deflections are 30°. The geometry includes fifteen slat brackets, three flap brackets, and the corresponding flap track fairings. The slat brackets in this work are referred to as the "aero"

---

[*]Aerospace Technologist, Computational AeroSciences Branch, Mail Stop 128, Senior Member, AIAA

[†]Aerospace Technologist, Computational AeroSciences Branch, Mail Stop 128

[‡]Aerospace Technologist, Computational AeroSciences Branch, Mail Stop 128, Associate Fellow, AIAA

[§]Aerospace Technologist, Computational AeroSciences Branch, Mail Stop 128, Fellow, AIAA

brackets as they were built for aerodynamic testing. Another set of "acoustic" brackets was built that are more realistic with a curved shape that would allow them to be stowed. However, the acoustic brackets, mounted on a separate slat, will not be tested until 2020. The wing semispan of the HL-CRM is 2.938 m (115.675 in), which corresponds to 10% of a large transport aircraft. The mean aerodynamic chord (MAC) of the HL-CRM wing is equal to 0.7 m (27.58 in) at a span station of 1.19 m (46.875 in).

NASA has developed an Active Flow Control version of the HL-CRM [14, 15], and both the conventional and flow control semispan models were tested in the 14x22 in 2018. The entry also included aeroacoustic measurements using an in-wall microphone array. In 2020, the model will be tested with the tunnel in the open-jet mode with an out-of-flow array. The HL-CRM will be used as a platform to evaluate slat noise-reduction concepts such as the slat-cove filler [16, 17] and slat-gap filler [18] at a technology readiness level near 5, which is higher than previous tests [16, 19]. Slat-cove fillers were tested on a trapezoidal-wing model [16] and the 26% 777 STAR model [19], but those treatments were incapable of being stowed. The HL-CRM tests will focus on deployable slat gap- and cove-fillers that will be constructed out of shape-memory alloys so that the slat can still be stowed. However, the HL-CRM slat will not articulate, and other testing will be used to evaluate additional structural aspects of the designs.

Computational simulations are being used to support the model development and to aid in the design of noise reduction devices. Although several computational fluid dynamics (CFD) codes are being employed in the overall effort, the commercial CFD software PowerFLOW® version 5.5b is being used to make aeroacoustic predictions of the noise from the HL-CRM. PowerFLOW® was used extensively during the design of the noise reduction technology applied to the Gulfstream aircraft model tested in the LaRC 14x22 subsonic tunnel [20, 21], and the noise predictions made before the experimental testing compared very well with the measurements. PowerFLOW® was also used for slat noise simulations involving the unswept 30P30N high-lift configuration from the BANC series of workshops [22]. Initial time-accurate simulations [23] of the flow over the HL-CRM in the landing configuration were completed in 2017 with PowerFLOW,® and the mean flow field was shown to be in reasonable agreement with the steady CFD results [24] from the FUN3D code [25]. Simulations of both a full-span slat and a part-span slat with a nacelle/pylon were performed. Surface pressure fluctuations and synthetic microphone array beamform maps were used to identify potential noise sources.

This paper presents further validation of the PowerFLOW® HL-CRM simulations through comparisons with experimental data collected in the 14x22 wind tunnel. Preliminary steady surface pressure and microphone array data from the experiment are used to obtain an initial assessment of the quality of the numerical simulations and to investigate the dominant noise sources on the model.

II. Simulation Methodology

The numerical simulations presented in this paper were performed using version 5.5b of the commercial CFD software PowerFLOW,® which is a compressible flow solver based originally on the three-dimensional 19 state (D3Q19) Lattice Boltzmann Model (LBM). The PowerFLOW® code represents LBM-based CFD technology developed over the last 30 years [26–30], and has been extensively validated for a wide variety of applications ranging from academic direct numerical simulations (DNS) to industrial flow problems in the fields of aerodynamics [31] and aeroacoustics [31–36]. In contrast to methods based on the Navier-Stokes (N-S) equations, LBM uses a simpler and more general physics formulation at the mesoscopic level [26]. The LBM equations recover the macroscopic hydrodynamics of the Navier-Stokes equations [37, 38] through the Chapman-Enskog expansion. The local formulation of the LBM equations allows a highly efficient implementation for distributed computations on thousands of processors. The low dissipation and dispersion properties of the numerical scheme produces aerodynamic and aeroacoustic results that are generally comparable to large eddy simulations obtained with traditional CFD solvers, as shown in Refs. [39] and [40], and demonstrated in the comparative study of flow over tandem cylinders by Lockard [41].

The classical LBM based on D3Q19 is typically valid in the low speed regime up to a local Mach number of 0.5. Recent extensions of the scheme [42–44] recover a fully unsteady compressible form of the Navier–Stokes equations. Applications of this new version at transonic conditions were presented in papers by Koenig and Fares [45] for the NASA CRM, and by Duda et al. [46] for a sweeping jet (fluidic) actuator operating at choked conditions. This newer version of the PowerFLOW® code has two options for higher-speed flows: the high-subsonic option for 0.5 < Mach < 0.9, and a transonic option for 0.9 < Mach < 2.0 that is approximately two times slower than the high-subsonic option. All of the results presented here were obtained using the high-subsonic option of the baseline solver. The local maximum time-averaged Mach number for the landing conditions under investigation is 0.6, which is low enough for the baseline solver. However, some transients with

a peak rms fluctuating Mach number will exceed 0.9, so the transonic version (not used here in the interest of computational efficiency) may produce somewhat improved results.

The PowerFLOW® code can be used to solve the Lattice-Boltzmann equation in a DNS mode [47], where all of the turbulent scales are spatially and temporally resolved. However, for most engineering problems at high Reynolds numbers, only the largest scales containing most of the energy are directly resolved, and the small scales are modeled. The current work uses the LBM Very Large Eddy Simulation (VLES) approach described in Refs. [28, 29] and [48].

The standard Lattice-Boltzmann boundary condition for no-slip or the specular reflection for free slip condition is generalized through a volumetric formulation [26, 27] near the wall for arbitrarily oriented surface elements (surfels) within the Cartesian volume elements (voxels). This formulation of the boundary condition on a curved surface cutting the Cartesian grid automatically conserves mass, momentum, and energy, and is compatible with the general second-order spatial accuracy of the underlying LBM numerical scheme. To reduce the resolution requirement near solid surfaces for high Reynolds number flows, a wall function is used to model the near wall region of the boundary layer [31, 33].

The Lattice-Boltzmann equation is solved on embedded Cartesian meshes, which are generated automatically within the flow solver on the basis of input specifications provided by the user. Variable resolution (VR) regions can be defined to allow for local mesh refinement of the grid by successive powers of two in each direction [26]. The PowerFLOW® code scales well on modern computer clusters consisting of thousands of processors, making it suitable for large scale applications.

III. Results

The computational domain is shown in Fig. 2(a), which is meant to represent the open-jet configuration of the 14x22. The outer boundaries are defined by a cube with sides that are roughly at 126 m (414 ft) from the model. A sphere with a radius of 125.5 m defines the simulation volume where freestream boundary conditions are defined. A turbulence intensity of 0.005 and length scale of 1 mm (0.0394 in) were used with a standard pressure of 101,325 Pa (14.7 psi) and static temperature of 15°C (519°R). An inviscid solid is defined below the model with an embedded viscous region (in red) representing the floor of the 14x22 test section. Other spheres (such as the pink one in the figure) prescribe variable resolution regions that refine the grid toward the model. The domain setup follows the standard best practices for PowerFLOW® simulations. The wind tunnel side walls and ceiling could be included, but they are neglected to avoid acoustic reflections. Some PowerFLOW® simulations [15] of the active flow control version of the HL-CRM have included the walls, but those calculations are solely focused on aerodynamic performance.

A planar view of a typical mesh is shown in Fig. 2(b). The increase in resolution near solid surfaces is obvious, but finer resolution was also specified to capture important flow features in the interior of the flow field. Figure 3 shows some of the VR regions on the upper and lower surfaces of the wing with a mean aerodynamic chord of 0.7 m. The red trailing edges have the finest resolution with a grid spacing of 0.144 mm. The next finest resolution is specified by the wireframe objects in yellow (0.288 mm) followed by those in orange (0.576 mm) and green (1.150 mm), respectively. Some of these regions are boxes and cylinders defined to enclose important flow features. In addition, the slat cove shear layer is encompassed by a VR region that was derived from isocontours obtained from earlier solutions on coarser grids. Important features from those earlier simulations were also identified from contours of the steady and unsteady surface pressure, surface and volume streamlines, and isosurfaces. Furthermore, noise source regions identified by synthetic microphone array analyses were also targeted for refinement. Localized refinement around the pylon, wing tip, slat, and flap are shown in Fig. 4. The resolution at the slat cusp, which appears black in Fig. 4(c), is 0.144 mm, and the region meant to resolve the slat shear layer has a grid spacing of 0.288 mm. One of the relatively straight aero slat brackets can also be seen in the figure. These brackets attach to the wing under slat surface (WUSS) further aft than realistic brackets. Cutouts for the brackets were not modeled, and the gaps around the brackets were taped in the experiment.

Initial PowerFLOW® simulations of the HL-CRM on a series of meshes [23] (with up to 900 million voxels) did not exhibit significant variations in the time-averaged surface pressure distributions, but even finer grids with targeted refinement exhibited significant changes, primarily as the separated flow region over the flap became better resolved. Several levels of refinement were tested without achieving a grid-independent solution, so a compromise resolution (0.288 mm within a 5 mm band) with an acceptable cost was selected that produced a steady surface pressure prediction on the slat and main element that was similar to those obtained with finer grids (0.144 mm within a 5 mm band). The refinement on the upper surface of the flap was generated using offsets from the flap surface and is needed to capture the separation on the flap.

The two meshes employed in this work are summarized in Table 1. The baseline part-span slat (PSS) configuration includes the nacelle/pylon, whereas they are removed for the full-span slat (FSS) configuration. The time advancement scheme within PowerFLOW® updates the solution in each cell only when needed, as determined on the basis of the cell size. The number of Fine Equivalent (FE) voxels denotes an estimate of the average number of cells that must be updated at each time step. However, when comparing grids with different minimum spacings, the number of time steps required to reach a specified time will vary linearly with the size of the smallest voxel. These calculations were performed at the NASA Advanced Supercomputing Division Pleiades cluster on 4000 Intel®Skylake processors with a run time of approximately five days. Acoustic post-processing took less than a day on 300 cores.

Table 1   Summary of Grid Parameters.

ID	Min spacing (mm)	Voxels ($\times 10^6$)	FE Voxels ($\times 10^6$)
Baseline PSS	0.144	1,304	431
FSS	0.144	1,012	338

All of the simulations have been run at landing conditions (slats deployed at an angle of 30° and the flaps at 37°) with a Mach number of 0.20, Reynolds number (based on the mean aerodynamic chord of 0.7 m or 27.58 in) of 3.27×10^6, and an angle of attack of 8.° This Reynolds number corresponds to the conditions for the 10% model as tested in the NASA LaRC 14x22 tunnel. However, to allow acoustic predictions, the simulations have been run with the semispan model mounted on a floor but without the wind tunnel walls and ceiling. Hence, the effective angle of attack is different between the experiments and simulations. By examining the pressure distributions between the simulations and experiments, the influence of the confinement on the effective angle of attack was estimated to be 1.° Hence, the experimental data corresponding to a 7° angle of attack will be used in all comparisons. A planned 2020 open-configuration test in the 14x22 will allow for a more direct comparison with the simulations both in terms of the flow blockage and acoustic reflections.

IV. Time-Averaged Surface Pressure Distribution

Views of time-averaged coefficient of pressure, C_p, contours are shown in Fig. 5 for both the Baseline PSS and FSS configurations. On the upper or suction side, the influence of the nacelle/pylon on the C_p distribution over the high-lift components is confined to a localized region of the span. The mean pressure distributions over the lower or compression sides of the two configurations are also similar to each other, with most of the differences being around the pylon and in its wake. Closeup views of the flap region from both simulations are shown in Fig. 5(e) and (f) with surface streamlines added as black lines. Both simulations exhibit major outboard flap separation indicated by the spanwise directed streamlines well upstream of the trailing edge of the flap. The entire span of the outboard flap shows some separation, but even some of the inboard flap around the flap bracket fairing is separated.

The computed surface pressures along selected planar cuts shown in Fig. 6 are compared with static pressure measurements obtained during the experiment. The spherical symbols represent the static pressure port locations on the model, and the planar cuts are indicated by the colored lines on the wing. The cuts were made with the flaps and slats in the stowed position, so a single plane does not cut through all of the ports when those elements are deployed. The parameter η is the distance in the spanwise direction normalized by the total semispan length.

Comparisons for the baseline PSS are shown in Fig. 7 with the most inboard cut at $\eta = 0.151$ in (a) and the most outboard cut at $\eta = 0.997$ in (f). To avoid overlapping lines, the x locations of the slat have been shifted upstream by 0.03 m (1.18 in) and the flap downstream by 0.02 m (0.787 in). In general, these time-averaged PowerFLOW® results are relatively insensitive to the grid resolution everywhere except on the flap and around the wing tip. The extent of the separated region on the flap was found to enlarge with grid refinement, and the track of vortices near the wing tip was also highly dependent on the grid. Once the grids in the simulations were fine enough to predict major separation on the flaps, further refinements affected the extent of the separation on the flap but did not have a major influence on the C_p distributions on the slat and main element.

The agreement between the experiment and PowerFLOW® is quite good at most of the spanwise stations, but the suction peak on the flap is generally underpredicted. Futhermore, the extent of the separated region on the outboard flap is slightly larger in the simulations at $\eta = 0.552$ and $\eta = 0.685$, and the suction on the upper surface of the slat at the two most inboard stations is overpredicted. Simulations were also run with an AoA of

4° and 12°, and these results are compared with the experiment in Figs. 8 and 9, respectively. The simulations at an AoA of 4° and 12° were run on slightly different geometries and grids than the 8° case. They were based on the as-designed geometry rather than the final as-built geometry. The main difference is in the inclusion of flap brackets, which are mostly hidden by the flap fairings. All of the observations made about the data at 8° are also true at the other angles of attack with the exception of Fig.9(b) where the simulation at 8° does not exhibit flap separation. At higher angles of attack, the flap does become more attached, but not quite as much as the simulation predicts. Despite some differences between the simulations and experiment, the overall trends are captured quite well, especially considering that the experiment was run in a closed-wall wind tunnel and the simulations were run in free air.

Similar comparisons for the FSS configuration at an AoA = 8° are presented in Fig. 10. The pressure distributions are similar to those from the PSS except at $\eta = 0.329$, which is the location of the nacelle/pylon. Another notable difference is at $\eta = 0.418$ where the flap separation in the simulations is increased, but otherwise the comparisons between simulation and experiment are equally good as those for the PSS. This is also true at 4° and 12° AoA as indicated in Figs. 11 and 12, respectively. In contrast to the PSS simulation at 12°, the simulations of the FSS does exhibit separation on the flap at $\eta = 0.685$ as indicated by the prominent plateau in the suction-surface C_p distribution.

V. Fluctuating Pressure Results

Contours of the root-mean-square (rms) of the fluctuating surface pressure from PowerFLOW® are shown in Fig. 13. Regions of high fluctuation levels may give rise to noise, although these plots do not provide any coherence information, which has just as much influence on the radiated noise as the amplitude. Nonetheless, examining regions with high fluctuation levels can provide some insight into how the aircraft is performing acoustically. In both the top and bottom views, the fluctuations around the nacelle/pylon are the highest and extend onto the upper surface of the wing. In addition to the unsteadiness around the slat break, one also observes relatively strong pressure fluctuations along the outboard slat cove. The other very prominent region of flow unsteadiness is on the upper surface of the outboard flap, where the flow separates. The unsteadiness in this region is most pronounced for the PSS case. The wake from the nacelle/pylon has an influence on the flap unsteadiness as do the flap fairings.

The slat bracket wakes are quite visible in the top views as regions of high surface pressure fluctuations as is the unsteadiness on the wing tip. Localized regions of increased fluctuation levels can be seen on the leading edges of the flaps in the vicinity of each of the flap fairings. The unsteadiness on the bottom surface of the model appears much more benign. The slat and flap coves exhibit higher fluctuation levels, with the slat cove outboard of the nacelle/pylon having the strongest unsteadiness. The wake of slat brackets impacting the leading edge of the main element gives rise to higher unsteadiness just as the flap brackets do with the leading edge of the flap. The flap and slat edges also have elevated levels, although they are not as apparent without zooming into those areas.

VI. Acoustics: Array Beamforming

Although the simulations indicate strong unsteadiness in several locations on the model, the rms levels discussed in the previous section include fluctuations at all frequencies. Some very low frequency oscillations of a predominantly aerodynamic nature may be present in the pressure signals and could well dominate the rms levels. These low-frequency oscillations may not contribute significantly to the noise annoyance, and, therefore, the scalar measure of broadband rms pressure fluctuations can be misleading from an acoustic perspective. Indeed, because only a small fraction of fluctuation energy is actually converted into acoustics, the rms pressure levels cannot be trusted to provide a reliable indication of the noise source locations at any frequency, whether low or high. One method to assess actual noise sources is through array beamforming. Contour maps of source strength provide information about the location of sources that is not available from the frequency spectra of surface pressure fluctuations. Array beamforming is typically used with experimental data, but the technique is now being successfully applied with numerical simulations [23, 49–51].

A methodology commonly used to make aeroacoustic predictions using CFD involves coupling the near-field solution from the CFD to an acoustic analogy such as the Ffowcs Williams and Hawking's equation [52] (FW-H). These predictions are often computed at the center of a microphone array and compared with array output. However, with a minimal increase in computational cost, the predictions can be made at all microphone locations in an array, and the signals processed in the same manner as the acoustic beamforming of experimental data.

Hence, the simulations provide synthetic array data that can be used with beamforming techniques. The far-field noise from the HL-CRM was calculated using the FW-H equation [52, 53] solver described by Bres [54]. Results were obtained using 0.4 seconds of pressure history on all solid surfaces on the model but not on the flat plate that serves as the floor. Reflections from the floor are not of interest and, when the tunnel is operated in the open-jet mode, sound absorbing foam will be used beneath the model.

Preliminary acoustic microphone array data from the 2018 HL-CRM test in the 14x22 will be compared against simulation data processed in an identical manner. The experimental data is considered preliminary because some corrections have not been applied, such as those for atmospheric absorption of the radiated noise. For the conditions of the experiment, atmospheric absorption could decrease the acoustic amplitude by up to 4 dB at 40 kHz. Furthermore, the array data have only been processed in 1/12 octaves, and the array shading and deconvolution algorithms have not been optimized. In addition, the measurements were made in a reverberant wind tunnel, which makes the interpretation of absolute levels even more difficult than in an anechoic environment. Nonetheless, the available data clearly identify the primary noise sources on the model and can be used toward an initial validation of the acoustic predictions from the simulations.

The position of the array relative to the model is shown in Fig. 14(a). The in-wall array is shown mounted on the South wall of the 14x22 wind tunnel, and the microphones are recessed behind a stainless steel mesh screen that is attached to a perforated plate. Although the 14x22 tunnel is capable of operating in an open-jet mode, the time to change the tunnel mode was prohibitive, so the in-wall array was employed instead. The entire acoustic portion of the test, from installation of the array and data acquisition equipment to the final acquisition, took place in one week. Recessing the microphones behind the screen provided sufficient shielding from pressure fluctuations associated with the wall boundary layer to allow the array to resolve frequencies as low as 1 kHz when diagonal removal was used. However, some contamination from the mesh and perforated plate was found above 40 kHz. The position of the array was dictated by mounting locations in the facility which placed the array slightly upstream of the the center of the wing. The 110-microphone array was 129.5 inches (3.29 m) from the wing centerline at the root, with an outer diameter (microphone to microphone) of 72 inches (1.83 m). The microphones were sampled at 196.608 kHz for 35 seconds, and both low- and high-pass filters were applied at 102 kHz and 400 Hz, respectively. A tanh-based shading algorithm was employed to exclude certain microphones based on the frequency so that sources appear similar in size across the frequency range. The shading also reduces the distances between the included microphones as the frequency increases, which helps to minimize the detrimental effects of decorrelation. The array data were processed using the AVEC beamforming code [55] that uses the CLEAN [56] deconvolution approach.

Integrated spectra are obtained from the beamform maps using the wing and slat integration regions identified in Fig. 14(b). After deconvolution, the maps give the power of the acoustic source spanning each cell in a 641×401 grid with 0.52 in (1.3 cm) resolution. A simple sum over the desired portion of the mesh yields the integrated spectra. The larger wing region is meant to include all airframe noise sources on the model while excluding mirror sources that appear below the model in the experiment. These mirror sources were prominent because of reflections in the tunnel and could easily be excluded because of their nonphysical location. However, some other sources that appear in random locations and are likely related to reflections from the North wall could not be eliminated. The smaller integration region in the figure is meant to isolate the noise from the slat, which is the focus of this investigation.

Integrated spectra from multiple tunnel runs at the same condition are shown in Fig. 15 for the two configurations. For the PSS, all of the repeat runs occurred on the same day, but those for the FSS occurred over two days. Overall, the repeatability is quite good except for differences around the very prominent tones around 10 kHz. Slat tones have been observed in many wind tunnel tests and are thought to be similar to Rossiter modes [57] in rectangular cavities. Slat tones have been linked to a feedback loop between instabilities in the slat cove shear layer and the acoustic signals they generate near the slat trailing edge [58, 59]. Because the spectral data in Fig. 15 has been processed in 1/12 octave bands, the multiple narrow-band-peak nature of the tones is not evident. Although the tones were nearly always present, their frequencies and amplitudes were sensitive to the flow conditions. The other prominent peak in the spectra is at 1.5 kHz, but beamform maps indicate that this source is actually from the facility and not the model. The broadband portion of the signal is about 1 dB higher in the PSS case, but the tones tended to be stronger with the FSS. Beyond 40 kHz, the spectra turn upwards, but this is because of contamination by the screen and perforated sheet. Some measurements were taken without the screen in place, and the signals above 40 kHz did not exhibit the anamoulous sources that were seen in beamform maps with the screen. Narrow band power spectral density spectra of the FSS and PSS configurations are compared in Fig. 16. These spectra were formed by averaging the signals of all of the microphones in the array. Even with the screen over the microphones, the spectrum is dominated by the

tunnel boundary layer and other facility noise. The broadband portion of the microphone spectra were relatively insensitive to the model configuration, indicating that noise from the model is not being represented in these autospectra. However, the slat tones are quite evident as they are up to 15 dB above the rest of the signal. For the particular PSS run shown in the figure, the tones are regularly spaced at 650 Hz intervals with the amplitude peaking at 10 kHz. The spacing is somewhat irregular but generally about the same for the FSS, and the primary tone is at 9.33 kHz. Some of the FSS runs also exhibit tones spaced at 325 Hz. The peaks are evident between 7.3 and 11.3 kHz with harmonics of the strongest tones visible between 17 and 21 kHz. These peaks may be an artifact of small-scale testing as no definitive flight measurements of such tones has been reported. No attempt was made to reduce or influence the tones during the limited duration of the 2018 test.

The effect of the angle of attack is examined in Fig. 17. Except at higher frequencies for the PSS, the broadband portion of the signal is relatively insensitive to the AoA. The elevated levels for the PSS at 11° are most likely a result of noise coming from the upper part of the wing reflecting off the tunnel walls, particularly the back wall. The primary sources in the beamform maps are actually off of the model and random, indicating that the propagation model used in the beamforming is failing and reflections are likely dominating. Even at 8°, a source above the nacelle/pylon is often visible above 15 kHz, so the separated region around the unslatted portion of the main element (which was shown to have high pressure fluctuations in Fig. 13(a)) is likely a strong radiator of noise. The tones are sensitive to the AoA both in terms of amplitude and frequency, and they do not scale with the Strouhal number as is typical of slat tones [59].

Spectra from the simulations are compared with the experiment in Fig. 18 for both the wing and slat integration regions. The corresponding beamform maps are in Figs. 19 and 20 for the experiment and the simulation, respectively. The data were processed in 1/12 octave bands with the results presented in terms of the model-scale frequency. The maps shown used a CLEAN [56] resolution of 4 in (0.1 m) so that the sources are visible, but the integrated levels were derived from maps with a resolution of zero, which reduces most of the sources to a single cell. The contour levels for each frequency are relative to the peak level for that map. Hence, the absolute levels cannot be compared across frequencies or cases. Nonetheless, the strengths of sources relative to the peak can be compared between different maps.

Fig. 18 indicates that below 7.1 kHz the spectral amplitude and shape from the simulation are in reasonable agreement with the experiment. The comparison is slightly better for the slat integration region. The beamform maps in Figs. 19 and 20 at 3 and 5 KHz show the primary source at these frequencies to be on the outboard end of the slat. The modulation in the contours is likely caused by the slat brackets as previous simulations without the brackets still showed a significant source in this region, but without the modulation. The slat brackets are significant sources themselves which are easily identified at 5 kHz. The outboard flap tip, flap brackets and fairings are secondary sources that can be seen at various frequencies. The wing tip and inboard flap tip are also expected to act as secondary sources, although they do not show up at any of the frequencies presented. The experimental maps around 10 kHz are dominated by the slat narrow band peaks, which are generated at different spanwise locations on the inboard end of the slat. The simulations still indicate the slat source near the tip to be strong, but additional slat sources inboard are also significant. Above 10 kHz the levels from the simulation are considerably higher than those from the experiment, partly because atmospheric absorption corrections have not been applied to the experimental data. At 15 kHz, both the experiment and simulation reveal the inboard slat tip to be dominant, but the simulations alone have it continuing to be prominent at higher frequencies. At 20 kHz the experiment is dominated by a harmonic of a slat tone, whereas the simulation shows an intense source around the outboard section of the main element cove. The unsteadiness in the separated region on the upper surface of the flap is giving rise to this source, but there is no indication of it in the experiment. Above 30 kHz, both the simulation and experiment indicate that sources on the slat reemerge as most prominent. In particular, the sources lie right on top of each of the brackets in the simulation beamform maps. At 40 kHz, the experimental map shows an arc of sources, which is an artifact of the mesh and perforated sheet. The contamination gets worse as the frequency increases, so 40 kHz is the highest frequency that can be interrogated. An improved in-wall design should be able to reduce this corruption, and the 2020 test will not use a screen at all.

Experimental CLEAN beamform maps for the baseline PSS configuration at an AoA of 8° and Mach number of 0.2 are shown in Fig. 21. The corresponding spectra can be seen as P3560 in Fig. 15(a). The noise analysis of a corresponding simulation is in progress but has not been completed. Compared with the maps for the FSS, the PSS has many more sources at apparently random locations. We speculate that there is more noise coming from the top of the model in this configuration, and the noise from these sources is reflecting off the walls and causing the contamination of the beamform maps. As was mentioned earlier, a prominent source is often visible above the nacelle, which may be attributed to radiation from the unslatted portion of the main

element. This fictitious source is easily identified at 15 kHz, but is also visible at 7.1 and 20 kHz. In general, the introduction of the nacelle/pylon has not affected the slat sources at 3 and 5 kHz, but the frequencies of the slat tones are different, suggesting that either the changes in the geometry or the spanwise flow influence the tones. The primary source at 10, 20, and 30 kHz appears to be centered on the middle bracket of the inboard slat. The narrow band spectra show multiple peaks between 7.3 and 11.3 kHz, so the dominant source at 10 kHz, and its harmonic, is associated with slat tones even though the location corresponds with a bracket. The source locations in this region may be misleading as the nacelle obscures a portion of the slat, and traditional beamforming cannot identify sources through an obstacle. Indeed, the sources at some frequencies that appear adjacent to the nacelle may be associated with the slat tips beside the pylon, where the unsteadiness was shown to be significant in the simulations.

VII. Conclusions

An initial evaluation of PowerFLOW® simulations of two separate variants of the HL-CRM with part-span and full-span slats, respectively, have been completed. Time-averaged results for the surface pressure compare reasonably well with those from an experiment conducted in the NASA LaRC 14x22 tunnel. The simulations were run in free-air, but the experiment was conducted in a closed test section. Therefore, an angle of attack adjustment was used in the comparisons. The primary area of difficulty for the simulations is in predicting the extent of flap separation, which is significant on the outboard flap. Nonetheless, the simulations capture the relevant features between an angle of attack of 4° and 12° . An aeroacoustic analysis of the full-span slat variant of the HL-CRM revealed that the slat cove and brackets are dominant noise sources on the model. Below 7 kHz model scale, both simulations and experiment are fairly consistent and identify multiple sources in the vicinity of the slat. Very intense slat tones were observed in the experiment between 7–12 kHz, but they were not predicted by the simulations. The physical origin of the slat related tones measured during the experiment remains to be determined. The baseline HL-CRM with a nacelle/pylon also exhibited dominant slat noise with tones, but the frequencies and amplitudes of the tones were different with the break in the slat. Furthermore, the broadband component of the noise from the baseline variant is louder, which is likely a result of flow unsteadiness around the pylon and nearby slat tips. This region is obscured by the nacelle, so traditional beamforming cannot isolate sources in this region.

Additional testing of the HL-CRM in the 14x22 is planned with the tunnel in the open-jet configuration with the walls and ceiling raised. Furthermore, the floor will be filled with foam to mitigate reflections. A traversing array of microphones will make measurements on the same side of the model as the in-wall array used in this work. The identical model variant will be tested before switching to several low-noise slat configurations. Although the simulations did not pick up the slat tones observed in the experiment, they did predict the broadband portion of the spectrum associated with the slat. Hence, the simulations are being used to aid the development of the slat noise reduction devices that will be tested in 2020. Furthermore, the effect of the noise reduction devices on the slat tones may provide some additional insight into the underlying physical mechanisms causing the narrow-band-peak phenomena.

Acknowledgment

References

[1] Hayes, J. A., Horne, W. C., Soderman, P. T., and Bent, P. H., "Airframe Noise Characteristics of a 4.7% Scale DC-10 Model," AIAA Paper 1997-1594, 1997.

[2] Storms, B. L., Ross, J. C., Horne, W. C., Hayes, J. A., Dougherty, R. P., Underbrink, J. R., Scharpf, D. F., and Moriarty, P. J., "An Aeroacoustic Study of an Unswept Wing with a Three-Dimensional High Lift System," NASA TM 112222, February 1998.

[3] Dobrzynski, W., Nagakura, K., Gehlhar, B., and Buschbaum, A., "Airframe Noise Studies on Wings with Deployed High-Lift Devices," AIAA Paper 1998-2337, 1998.

[4] Storms, B. L., Hayes, J. A., Moriarty, P. J., and Ross, J. C., "Aeroacoustic Measurements of Slat Noise on a Three-Dimensional High-Lift System," AIAA Paper 1999-1957, 1999.

[5] Choudhari, M. M., Lockard, D. P., Macaraeg, M. G., Singer, B. A., Streett, C. L., Neubert, G. R., Stoker, R. W., Underbrink, J. R., Berkman, M. E., Khorrami, M. R., and Sadowski, S. S., "Aeroacoustic Experiments in the Langley Low-Turbulence Pressure Tunnel," NASA TM 211432, February 2002.

[6] Mendoza, F., and Brooks, T., "Aeroacoustic Measurements of a Wing/Slat Model," AIAA Paper 2002-2604, 2002.

[7] Terracol, M., Manoha, E., and Lemoin, B., "Noise Sources Generation in a Slat Cove: Hybrid Zonal RANS/LES Simulation and Dedicated Experiment," AIAA Paper 2011-3203, 2011.

[8] Chow, L. C., Mau, K., and Remy, H., "Landing Gears and High Lift Devices Airframe Noise Research," AIAA Paper 2002-2408, 2002.

[9] Lacy, D. S., and Sclafani, A. J., "Development of the High Lift Common Research Model (HL-CRM): A Representative High Lift Configuration for Transonic Transports," AIAA Paper 2016-0308, 2016.

[10] AIAA Drag Prediction Workshop Web Site: https://aiaa-dpw.larc.nasa.gov/, retrieved 17 March, 2019.

[11] NASA Common Research Model Web Site: https://commonresearchmodel.larc.nasa.gov/, retrieved 17 March, 2019.

[12] AIAA Geometry and Mesh Generation Web Site: http://www.pointwise.com/gmgw/, retrieved 17 March, 2019.

[13] AIAA High Lift Prediction Workshop: https://hiliftpw.larc.nasa.gov/, retrieved 17 March, 2019.

[14] Lin, J. C., Melton, L. G., Hannon, J. A., Andino, M. Y., Koklu, M., Paschal, K. B., and Vatsa, V. N., "Wind Tunnel Testing of Active Flow Control on High Lift Common Research Model," to be presented at the 2019 AIAA AVIATION meeting in Dallas, TX, 2019.

[15] Vatsa, V. N., Duda, B. M., Lin, J. C., Pack, L. G., and O'Connell, M. D., "Comparative Study of Active Flow Control Strategies for Lift Enhancement of a Simplified High-Lift Configuration," to be presented at the 2019 AIAA AVIATION meeting in Dallas, TX, 2019.

[16] Streett, C. L., Casper, J., Lockard, D. P., Khorrami, M. R., Stoker, R., Elkoby, R., Wenneman, W., and Underbrink, J., "Aerodynamic Noise Reduction for High-Lift Devices on a Swept Wing Model," AIAA Paper 2006-0212, 2006.

[17] Scholten, W. D., Hartl, D. J., Turner, T. L., and Kidd, R. T., "Development and Analysis-Driven Optimization of Superelastic Slat-Cove Fillers for Airframe Noise Reduction," *AIAA Journal*, Vol. 54, No. 3, 2016, pp. 1078–1094.

[18] Turner, T. L., and Long, D. L., "Development of a SMA-Based, Slat-Gap Filler for Airframe Noise Reduction," AIAA Paper 2015-0730, 2015.

[19] Horne, W. C., Burnside, N. J., Soderman, P. T., Jaeger, S. M., Reinero, B. R., James, K. D., and Arledge, T. K., "Aeroacoustic Study of a 26%-Scale Semispan Model of a Boeing 777 Wing in the NASA Ames 40- by 80-Foot Wind Tunnel," NASA TP 2004-212802, October 2004.

[20] Fares, E., Casalino, D., and Khorrami, M., "Evaluation of Airframe Noise Reduction Concepts via Simulations Using a Lattice Boltzmann Approach," AIAA Paper 2015-2988, 2015.

[21] Khorrami, M. R., Humphreys, W. M., Lockard, D. P., and Ravetta, P. A., "An Assessment of Flap and Main Landing Gear Noise Abatement Concepts," AIAA Paper 2015-2978, 2015.

[22] Choudhari, M. M., and Lockard, D. P., "Assessment of Slat Noise Predictions for 30P30N High-Lift Configuration from BANC-III Workshop," AIAA Paper 2015-2844, 2015.

[23] Lockard, D. P., Choudhari, M. M., Vatsa, V. N., O'Connell, M. D., Duda, B. M., and Fares, E., "Noise Simulations of the High-Lift Common Research Model," AIAA Paper 2017-3362, 2017.

[24] Rivers, M., Hunter, C., and Vatsa, V., "Computational Fluid Dynamic Analyses for the High-Lift Common Research Model Using the USM3D and FUN3D Flow Solvers," AIAA Paper 2017-0320, 2017.

[25] Biedron, R. T., Derlaga, J. M., Gnoffo, P. A., Hammond, D. P., Jones, W. T., Kleb, B., Lee-Rausch, E. M., Nielsen, E. J., Park, M. A., Rumsey, C. L., Thomas, J. L., , and Wood, W. A., "FUN3D Manual: 12.4," NASA TM 2014-218179, March 2014.

[26] Chen, H., "Volumetric Formulation of the Lattice Boltzmann Method for Fluid Dynamics: Basic Concept," *Physical Review A*, Vol. 58, 1998, pp. 3955–3963.

[27] Chen, H., Teixeira, C., and Molvig, K., "Realization of Fluid Boundary Conditions via Discrete Boltzmann Dynamics," *Intl. J. Mod. phys. C*, Vol. 9, No. 8, 1998, pp. 1281–1292.

[28] Yakhot, V., and Orszag, S., "Renormalization Group Analysis of Turbulence. I. Basic Theory," *J. Sci. Comput.*, Vol. 1, No. 2, 1986, pp. 3–51.

[29] Chen, H., Kandasamy, S., Orszag, S., Shock, R., Succi, S., and Yakhot, V., "Extended Boltzmann Kinetic Equation for Turbulent Flows," *Science*, Vol. 301, No. 5633, 2003, pp. 633–636.

[30] Chen, S., and Doolen, G., "Lattice Boltzmann Method for Fluid Flows," *Annu. Rev. Fluid Mech.*, Vol. 30, 1998, pp. 329–364.

[31] Fares, E., and Nölting, S., "Unsteady Flow Simulation of a High-Lift Configuration using a Lattice Boltzmann Approach," AIAA Paper 2011-869, 2011.

[32] Khorrami, M., Fares, E., and Casalino, D., "Towards Full-Aircraft Airframe Noise Prediction: Lattice-Boltzmann Simulations," AIAA Paper 2014-2481, 2014.

[33] Fares, E., "Unsteady Flow Simulation of the Ahmed Reference Body using a Lattice Boltzmann Approach," *Comput. Fluids*, Vol. 35, No. 8-9, 2006, pp. 940–950.

[34] Brès, G., Fares, E., Williams, D., and Colonius, T., "Numerical Simulations of the Transient Flow Response of a 3D, Low-Aspect-Ratio Wing to Pulsed Actuation," AIAA Paper 2011-3440, 2011.

[35] Brès, G., Freed, D., Wessels, M., Nöelting, M., and Pérot, F., "Flow and Noise Predictions for Tandem Cylinder Aeroacoustic Benchmark," *Physics of Fluids*, Vol. 24, No. 3, 2012, 036101. Http://dx.doi.org/10.1063/1.3685102.

[36] Casalino, D., Ribeiro, A., and Fares, E., "Facing Rim Cavities Fluctuation Modes," *Journal of Sound and Vibration*, Vol. 333, No. 13, 2014, pp. 2812–2830.

[37] Chen, H., Chen, S., and Matthaeus, W., "Recovery of the Navier-Stokes Equations Using a Lattice-gas Boltzmann Method," *Physical Review A*, Vol. 45, 1992, pp. 5339–5342.

[38] Qiana, Y. H., D'Humiéres, D., and Lallemand, P., "Lattice BGK Models for Navier-Stokes Equations," *Europhysics Letters*, Vol. 17, 1992, pp. 479–484.

[39] Marié, S., Ricot, D., and Sagaut, P., "Comparison between Lattice Boltzmann Method and Navier-Stokes High Order Schemes for Computational Aeroacoustics," *J. of Computational Physics*, Vol. 228, 2009, pp. 1056–1070.

[40] Brès, G., Pérot, F., and Freed, D., "Properties of the Lattice-Boltzmann Method for Acoustics," AIAA Paper 2009-3395, 2009.

[41] Lockard, D., "Summary of the Tandem Cylinder Solutions from the Benchmark Problems for Airframe Noise Computations-I Workshop," AIAA Paper 2011-353, 2011.

[42] Shan, X., Yuvan, X.-F., and Chen, H., "Kinetic Theory Representation of Hydrodynamics: a Way Beyond the Navier-Stokes Equation," *Physics. Rev. Lett.*, Vol. 80, 1998, pp. 65–88.

[43] Zhuo, C., Zhong, C., Li, K., Xiong, S., Chen, X., and Cao, J., "Application of Lattice Boltzmann Method to Simulation of Compressible Turbulent Flow," *Commun. Comput. Physics*, Vol. 8, 2010, pp. 1208–1223.

[44] Fares, E., Wessels, M., Li, Y., Gopalakrishnan, P., Zhang, R., Sun, C., Gopalaswamy, N., Roberts, P., Hoch, J., and Chen, H., "Validation of a Lattice Boltzmann Approach for Transonic and Supersonic Simulations," AIAA Paper 2014-0952, 2014.

[45] Koenig, B., and Fares, E., "Validation of a Transonic Lattice-Boltzmann Method for the NASA Common Research Model," AIAA Paper 2016-2023, 2016.

[46] Duda, B. M., Fares, E., Wessels, M., and Vatsa, V., "Unsteady Flow Simulation of a Sweeping Jet Actuator Using a Lattice-Boltzmann Method," AIAA Paper 2016-1818, 2016.

[47] Li, Y., Shock, R., and Chen, H., "Numerical Study of Flow Past an Impulsively Started Cylinder by Lattice Botzmann Method," *J. Fluid Mech.*, Vol. 519, 2004, pp. 273–300.

[48] Chen, H., Orszag, S., Staroselsky, I., and Succi, S., "Expanded Analogy between Boltzmann Kinetic Theory of Fluid and Turbulence," *J. Fluid Mech.*, Vol. 519, 2004, pp. 301–314.

[49] Marotta, T. R., Lieber, L. S., and Dougherty, R. P., "Validation of Beamforming Analysis Methodology with Synthesized Acoustic Time History Data: Sub-Scale Fan Rig System," AIAA Paper 2014-3068, 2014.

[50] Lockard, D. P., Humphreys, W. M., Khorrami, M. R., Fares, E., Casalino, D., and Ravetta, P. A., "Comparison of Computational and Experimental Microphone Array Results for an 18%-Scale Aircraft Model," AIAA Paper 2015-2990, 2015.

[51] Lockard, D. P., Humphreys, W. M., Khorrami, M. R., Fares, E., Casalino, D., and Ravetta, P. A., "Comparison of Computational and Experimental Microphone Array Results for an 18%-Scale Aircraft Model," *International Journal of Acoustics*, Vol. 16, No. 4-5, 2017, pp. 358–381.

[52] Ffowcs Williams, J. E., and Hawkings, D. L., "Sound Generation by Turbulence and Surfaces in Arbitrary Motion," *Philosophical Transactions of the Royal Society*, Vol. A264, No. 1151, 1969, pp. 321–342.

[53] Najafi-Yazdi, A., Bres, G. A., and Mongeau, L., "An Acoustic Analogy Formulation for Moving Sources in Uniformly Moving Media," *Proceedings of the Royal Society of London, Series A*, Vol. 467, No. 2125, 2011, pp. 144–165.

[54] Brès, G. A., Wessels, M., and Nöelting, S., "Tandem Cylinder Noise Predictions Using Lattice Boltzmann and Ffowcs Williams – Hawkings Methods," AIAA Paper 2010-3791, 2010.

[55] AVEC Frequency Domain Beamforming Software, Ver 4.40, AVEC, Inc., Blacksburg, VA, URL: http://www.avec-engineering.com/products.html, retrieved 17 March, 2019.

[56] Sijtsma, P., "CLEAN Based on Spatial Source Coherence," AIAA Paper 2007-3436, 2007.

[57] Rossiter, J. E., "Wind-tunnel Experiments on the Flow over Rectangular Cavities at Subsonic and Transonic Speeds," Aeronautical Research Council Reports and Memoranda No. 3438, 1964.

[58] Terracol, M., Manoha, E., and Lemoine, B., "Investigation of the Unsteady Flow and Noise Generation in a Slat Cove," *AIAA Journal*, Vol. 54, No. 2, 2016, pp. 469–489.

[59] Pascioni, K. A., and Cattafesta, L. N., "Unsteady Characteristics of a Slat-Cove Flow Field," *Physical Review Fluids*, Vol. 3, 2018, pp. 2842–2847. doi:10.1103/PhysRevFluids.3.034607.

(a) Baseline PSS

(b) FSS

Fig. 1   HL-CRM configurations in the 14x22 wind tunnel.
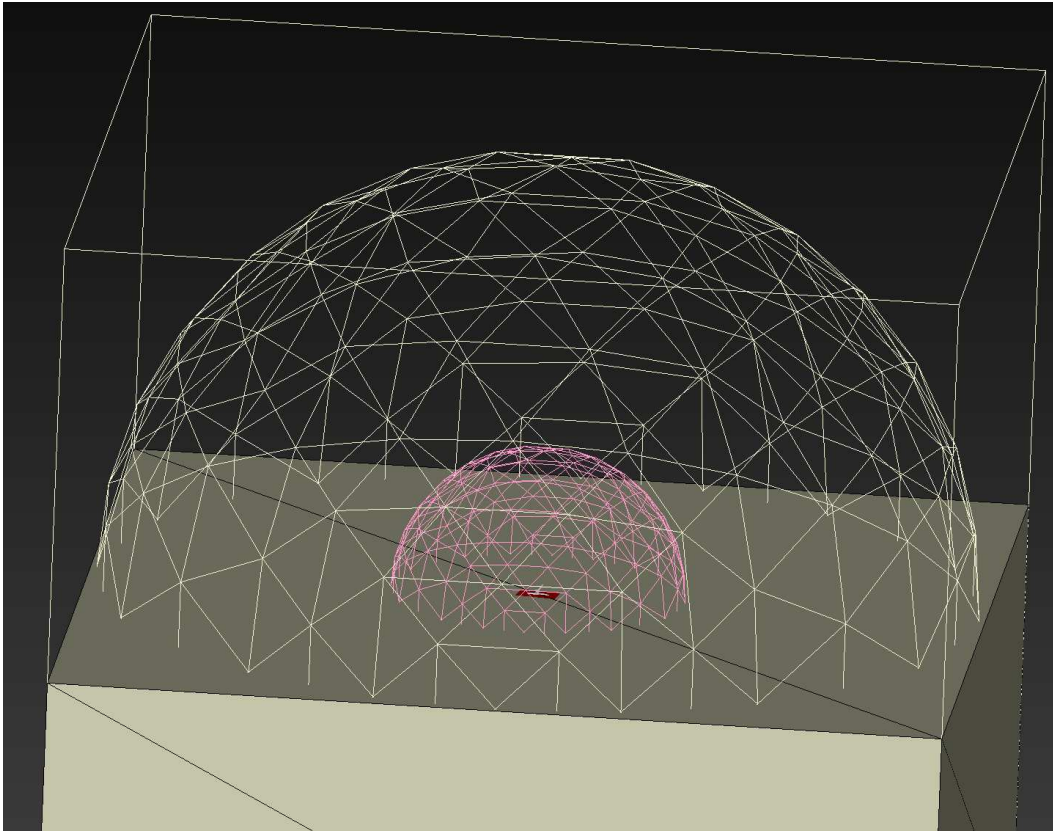
(a) Computational Domain
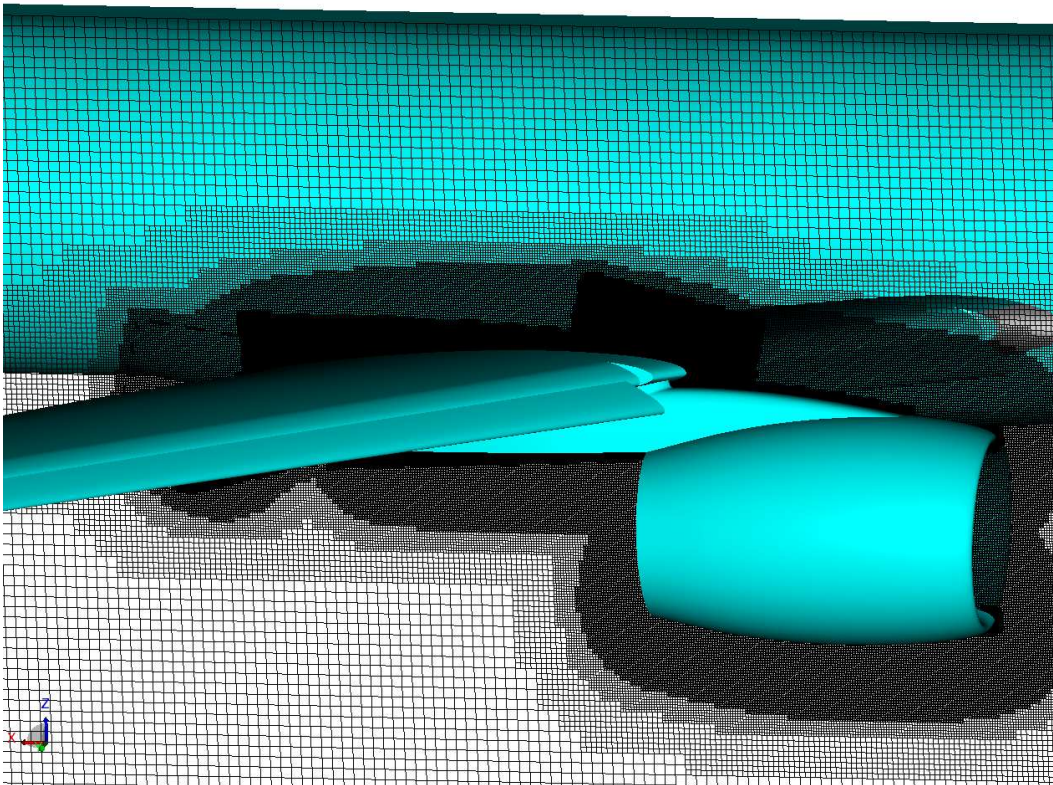
(b) Grid

Fig. 2   Computational domain and PowerFLOW® grid on a planar cut through the Baseline PSS configuration.
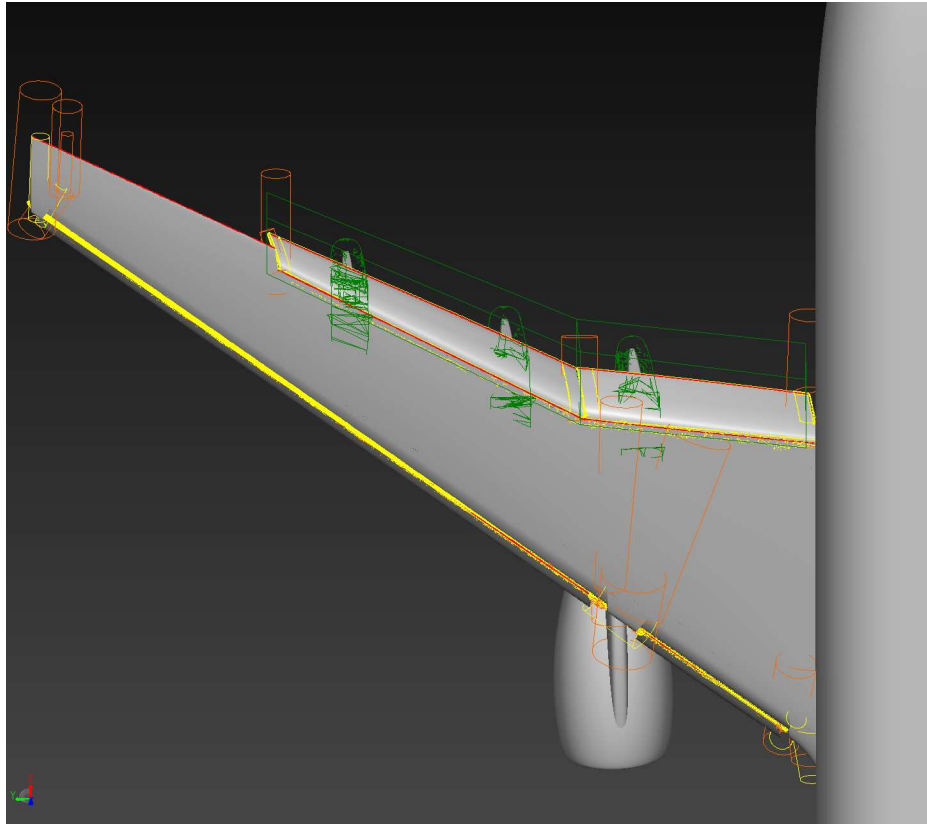
(a) Wing upper surface (top view)
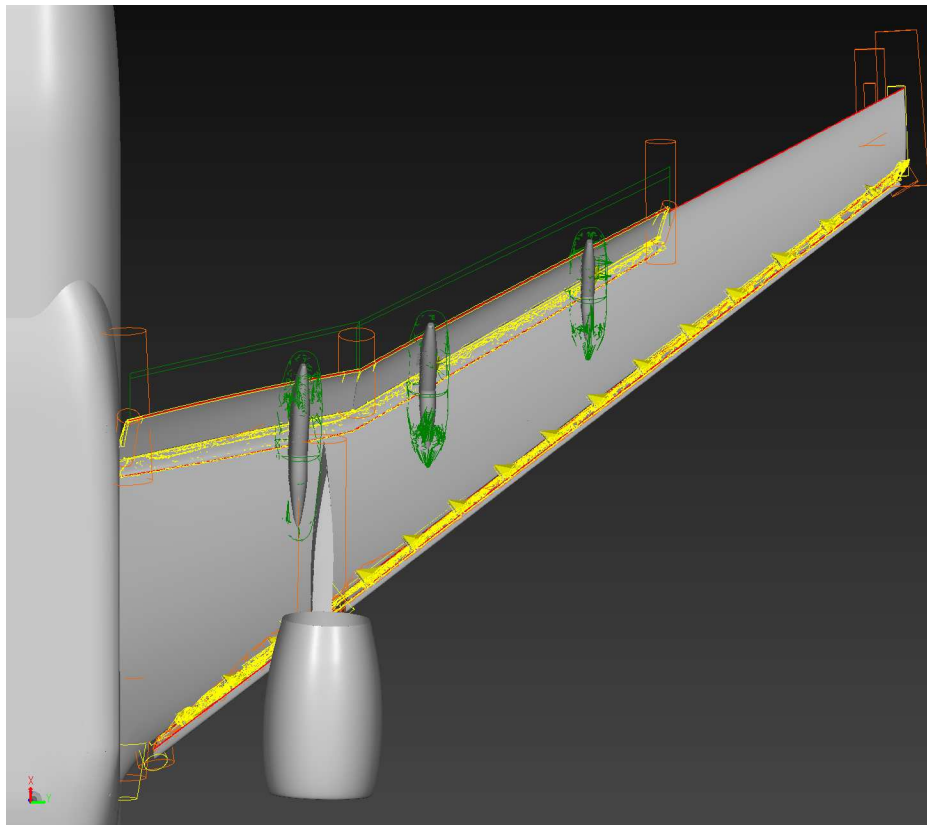
(b) Wing lower surface (bottom view)

Fig. 3   Selected VR regions on the HL-CRM.

(a) Pylon

(b) Wing tip

Aero bracket
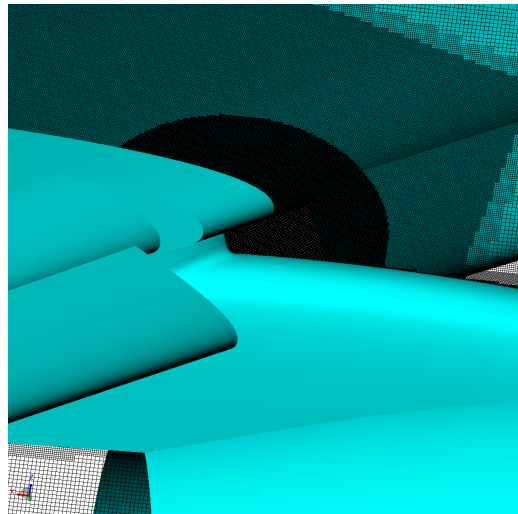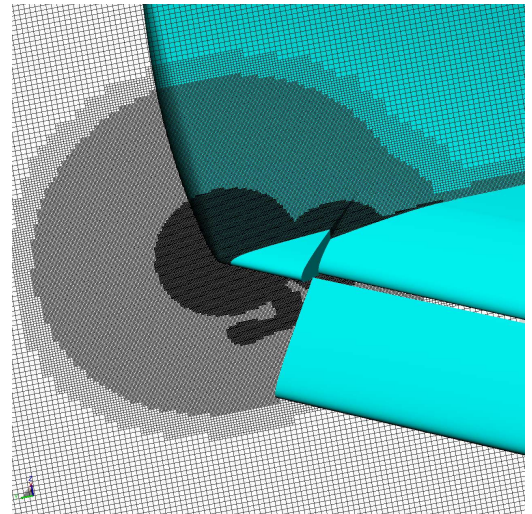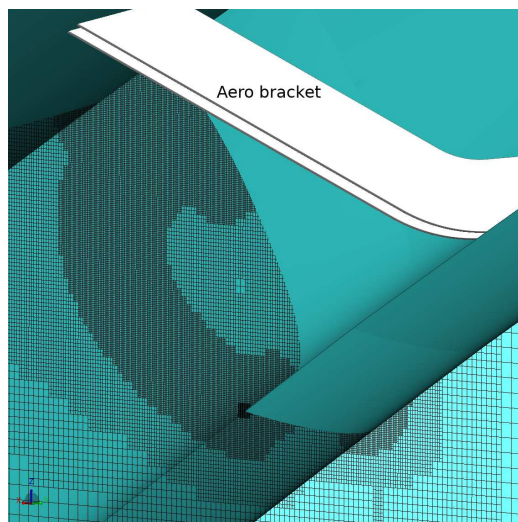
(c) Slat
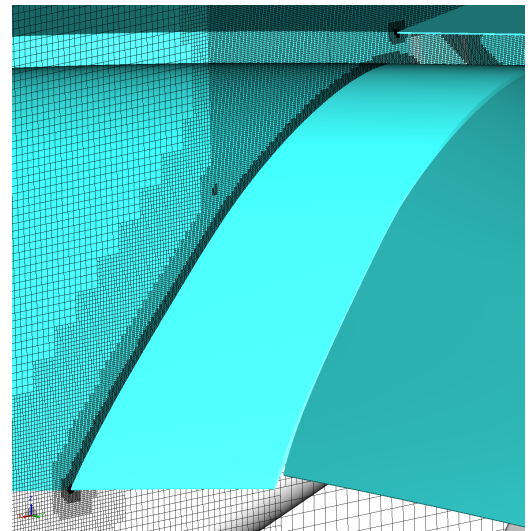
(d) Flap

Fig. 4   PowerFLOW® grid on planes through the HL-CRM Baseline PSS configuration.
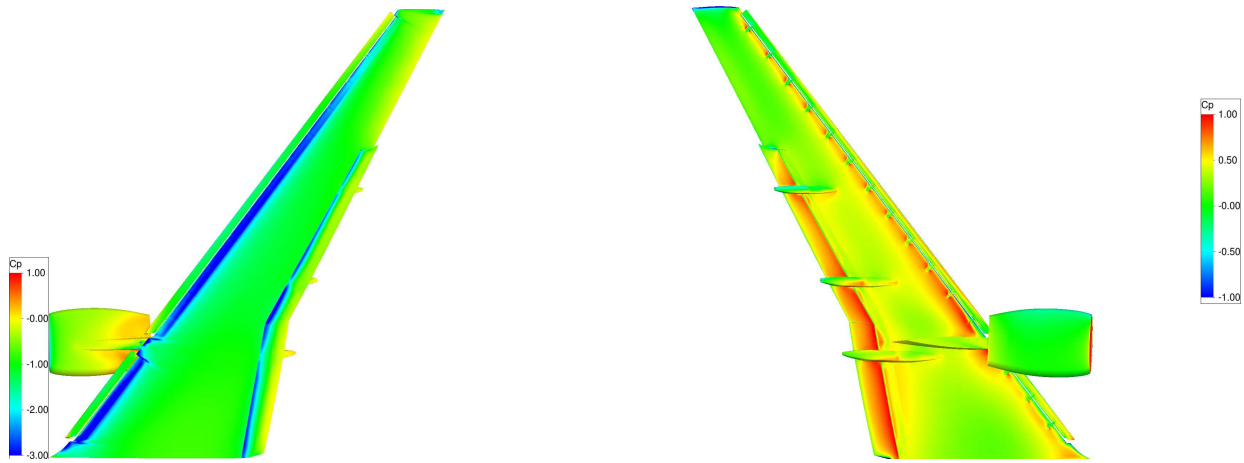
(a) PSS upper surface (top view)

(b) PSS lower surface (bottom view)
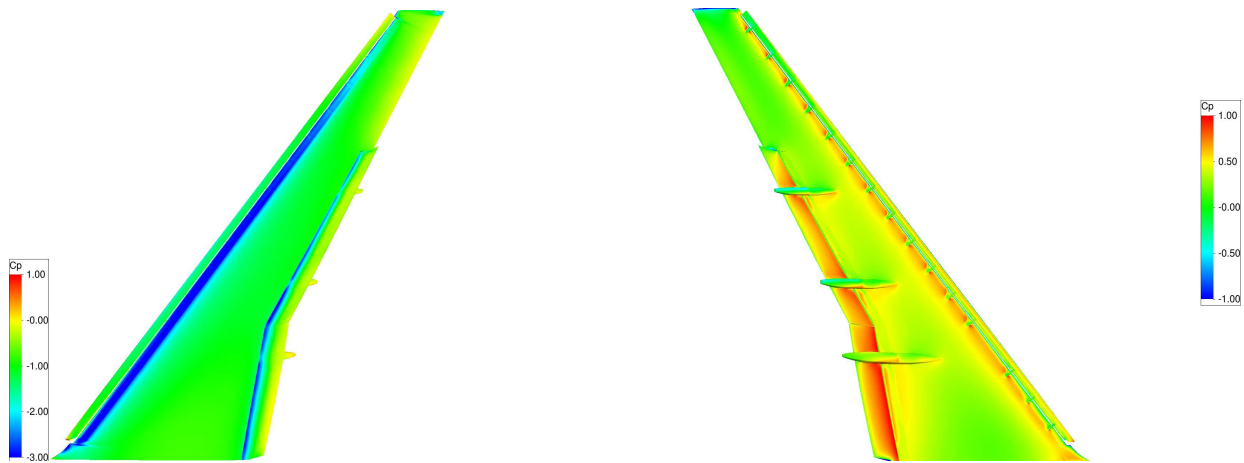
(c) FSS upper surface (top view)

(d) FSS lower surface (bottom view)
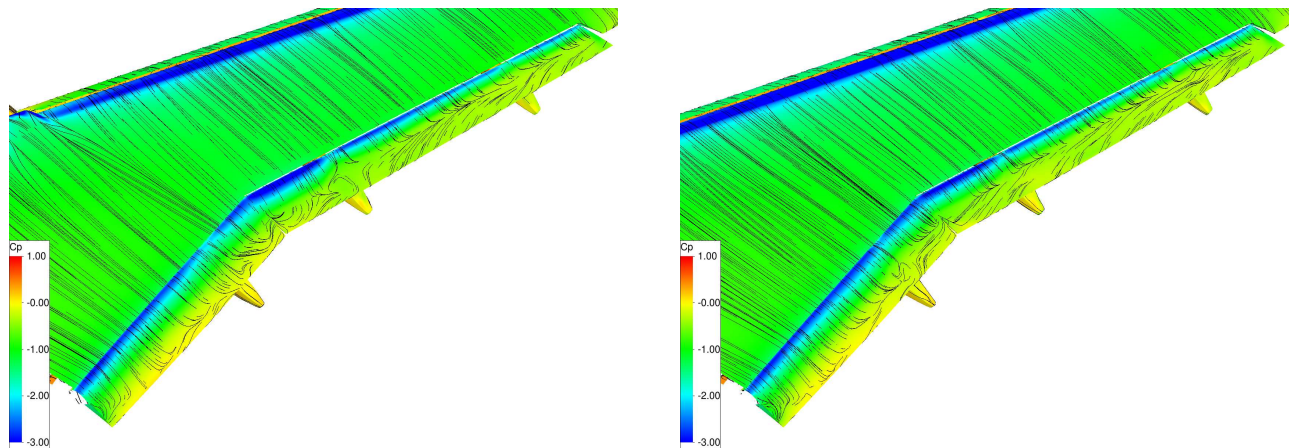
(e) PSS flaps (top view)

(f) FSS flaps (top view)

Fig. 5   Contours of mean C_p on the HL-CRM surface. Black lines indicate streamlines.
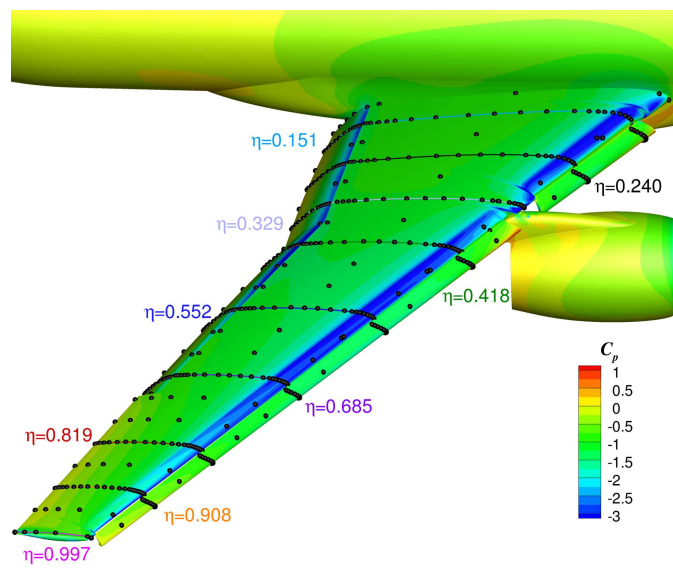
Fig. 6   Planar wing cuts used for comparisons with experimental data. Symbols indicate static pressure port locations. The flap beak is at $\eta = 0.37$, and the outboard flap extends to $\eta = 0.72$.
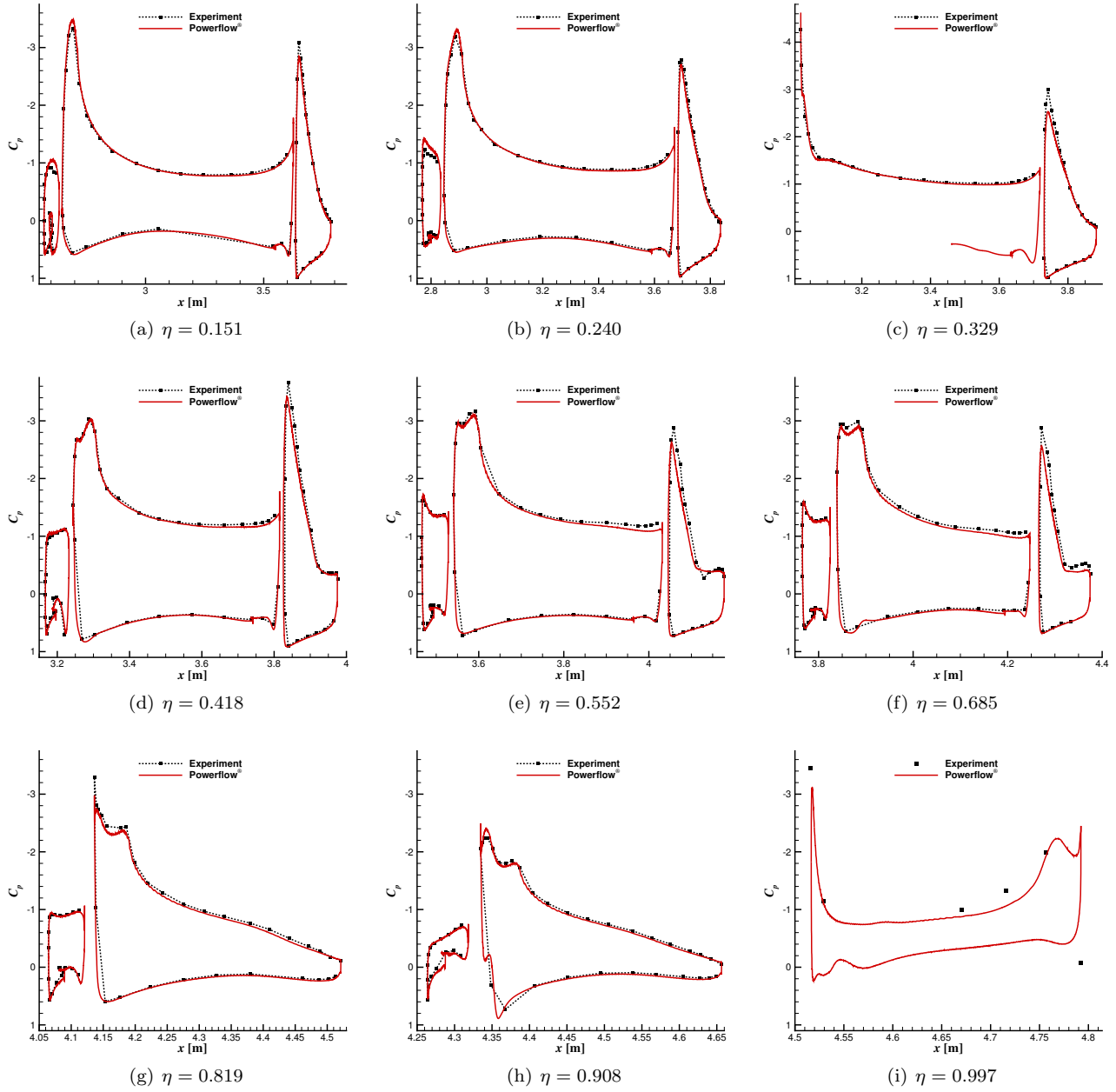
Fig. 7 Surface C_p distributions along cuts through the HL-CRM wing for the baseline PSS configuration at $M = 0.2$. **14x22 experiment at AoA = 7° with closed walls and simulations at AoA = 8° in free air.**

Fig. 8 Surface C_p distributions along cuts for the baseline PSS configuration at $M = 0.2$. **14x22 experiment at AoA $= 3°$ with closed walls and simulations at AoA $= 4°$ in free air.**

(a) $\eta = 0.151$ (b) $\eta = 0.240$ (c) $\eta = 0.418$

(d) $\eta = 0.552$ (e) $\eta = 0.685$ (f) $\eta = 0.908$

Fig. 9 Surface C_p distributions along cuts for the baseline PSS configuration at $M = 0.2$. **14x22 experiment at AoA $= 11°$ with closed walls and simulations at AoA $= 12°$ in free air.**

(a) $\eta = 0.151$ (b) $\eta = 0.240$ (c) $\eta = 0.418$

(d) $\eta = 0.552$ (e) $\eta = 0.685$ (f) $\eta = 0.908$

(a) $\eta = 0.151$

(b) $\eta = 0.240$

(c) $\eta = 0.329$

(d) $\eta = 0.418$

(e) $\eta = 0.552$

(f) $\eta = 0.685$

(g) $\eta = 0.819$

(h) $\eta = 0.908$

(i) $\eta = 0.997$
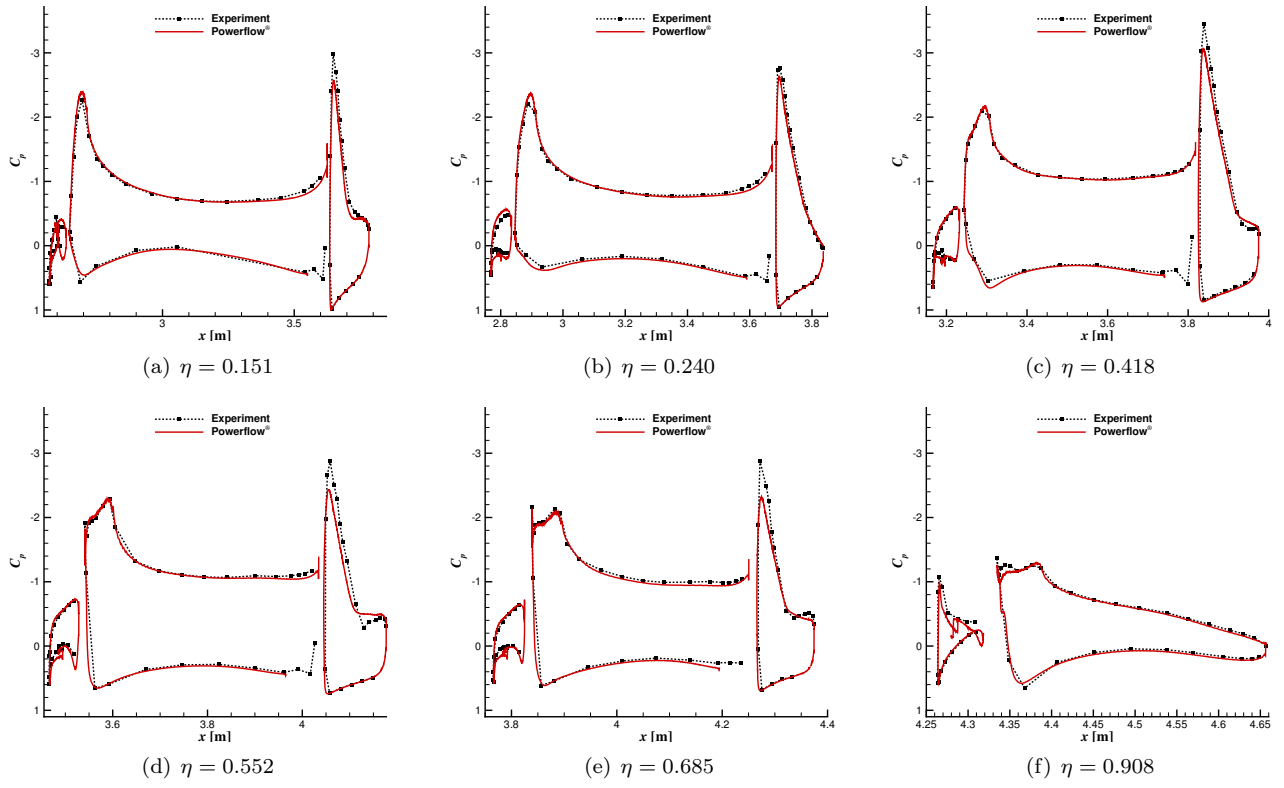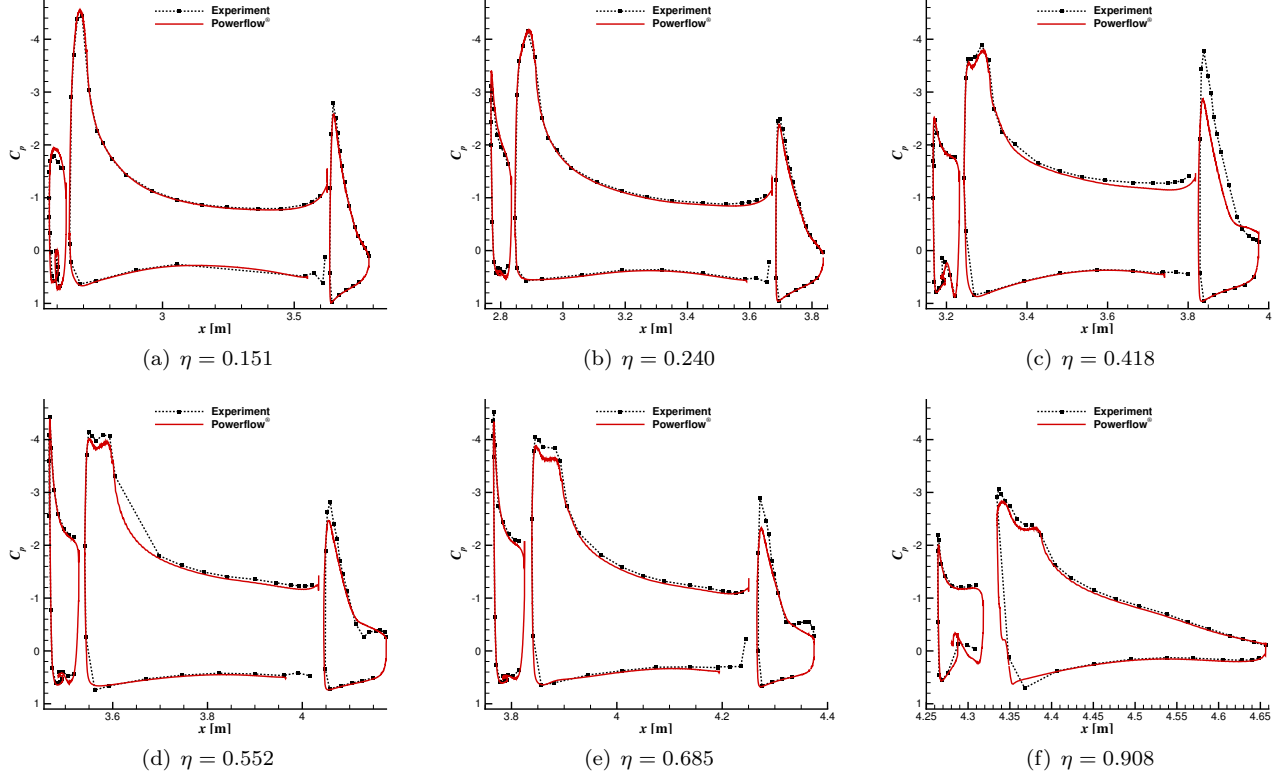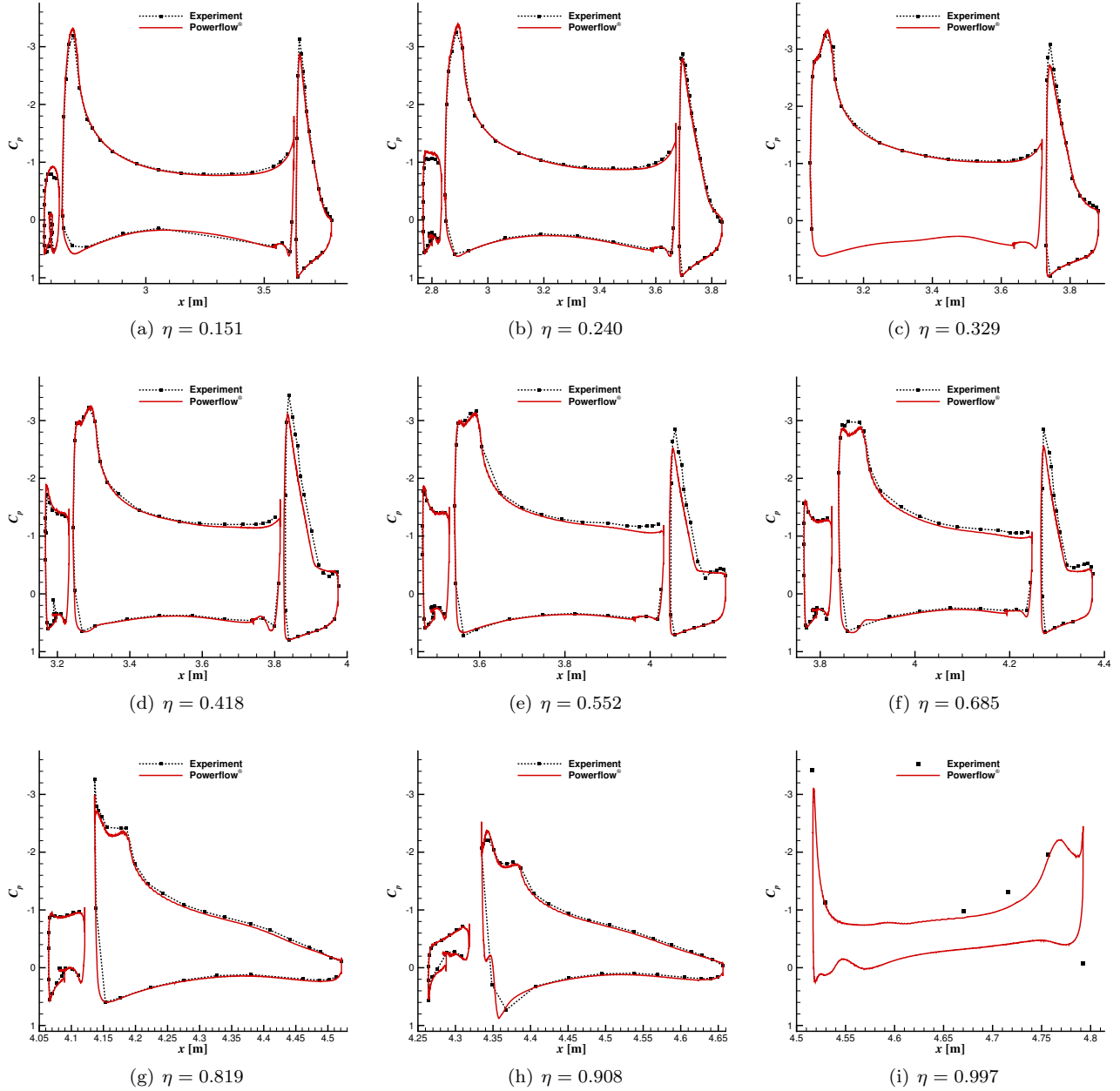
Fig. 10 Surface C_p distributions along cuts for the FSS configuration at $M = 0.2$. **14x22 experiment at AoA $= 7°$ with closed walls and simulations at AoA $= 8°$ in free-air.**
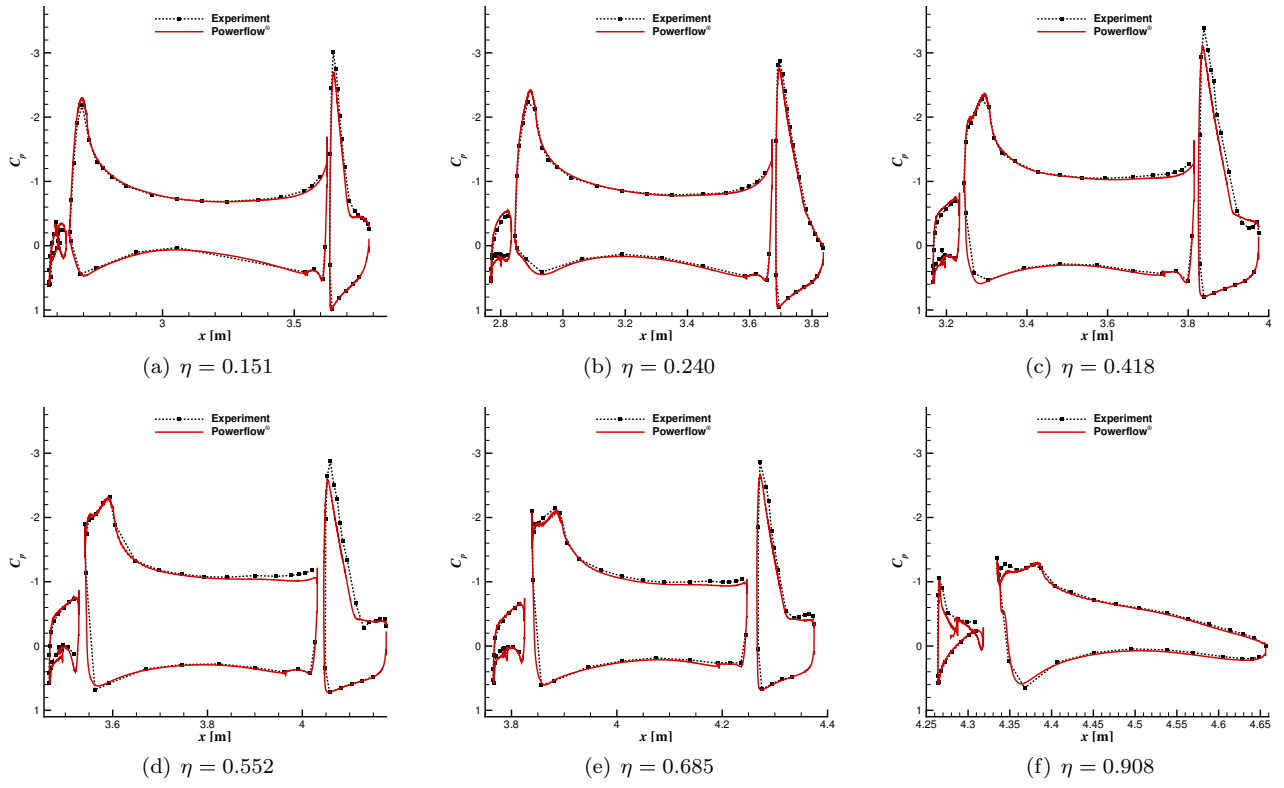
Fig. 11 Surface C_p distributions along cuts for the FSS configuration at $M = 0.2$. **14x22 experiment at AoA = 3° with closed walls and simulations at AoA = 4° in free air.**

Fig. 12 Surface C_p distributions along cuts for the FSS configuration at $M = 0.2$. **14x22 experiment at AoA = 11° with closed walls and simulations at AoA = 12° in free air.**

(a) PSS upper surface (top view)

(b) PSS lower surface (bottom view)

(c) FSS upper surface (top view)

(d) FSS lower surface (bottom view)
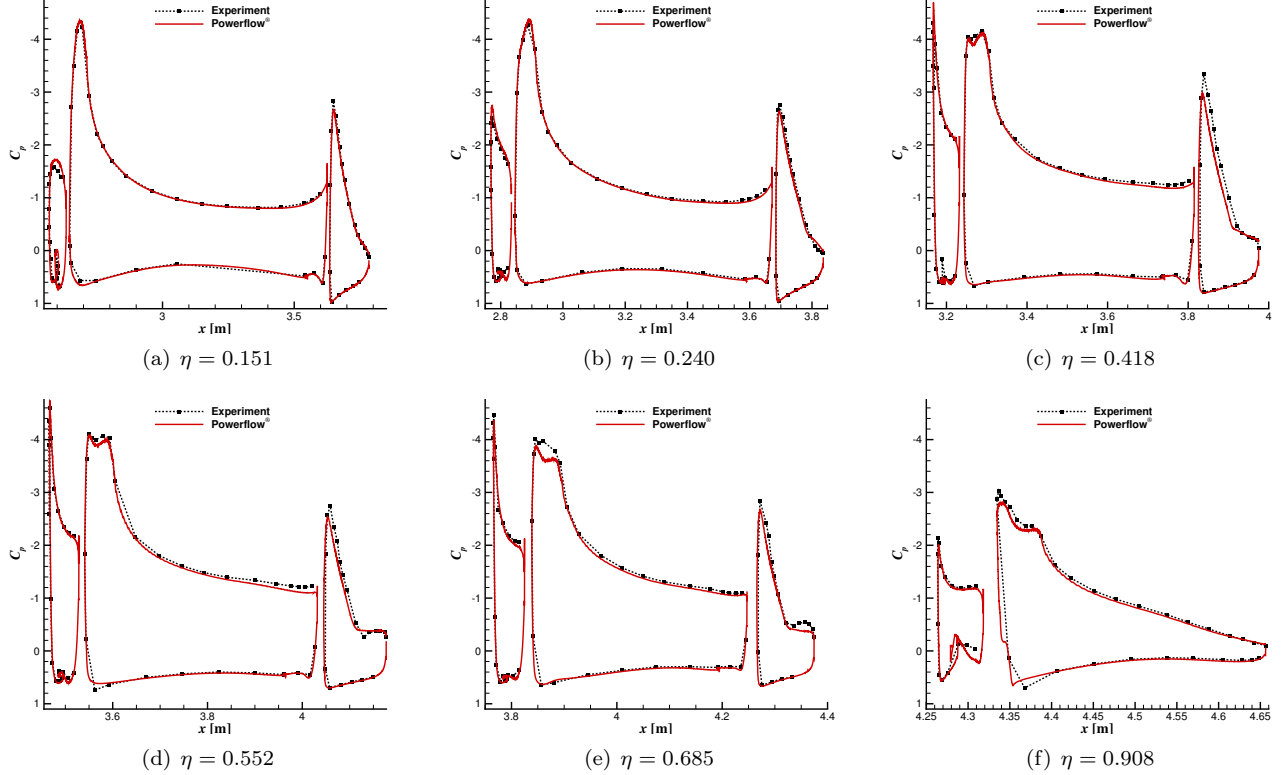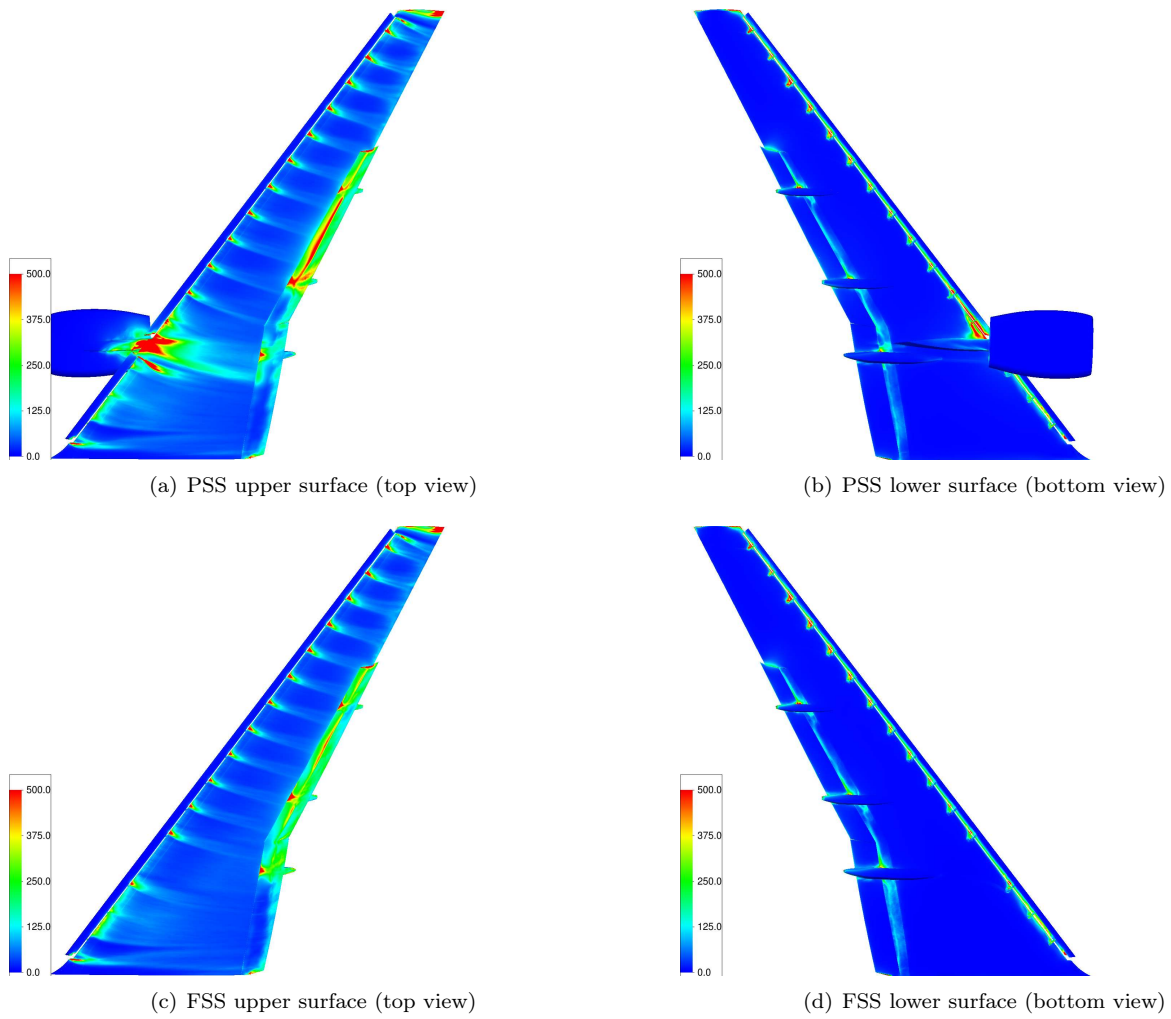
Fig. 13   Contours of surface pressure fluctuations (p'_{rms} in Pa) on the HL-CRM.
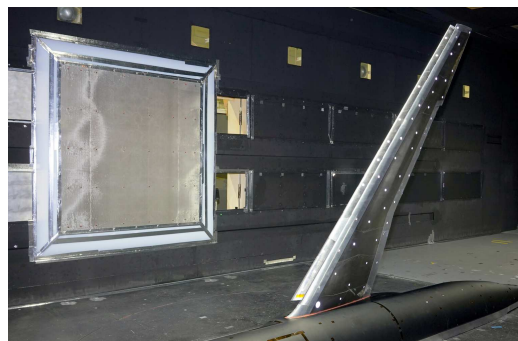
(a) Microphone Array
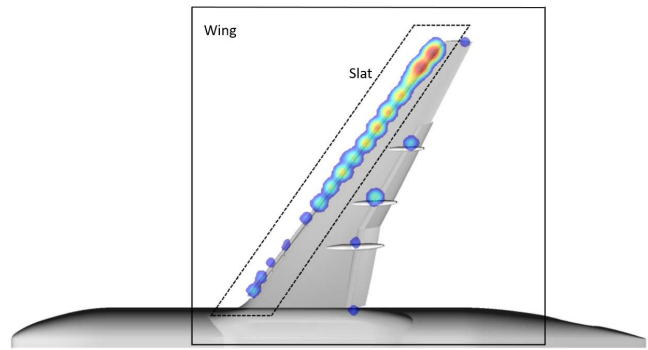
(b) Integration Regions

Fig. 14   Microphone array in the 14x22 on the suction side of the FSS HL-CRM and the integration regions used with beamform results.
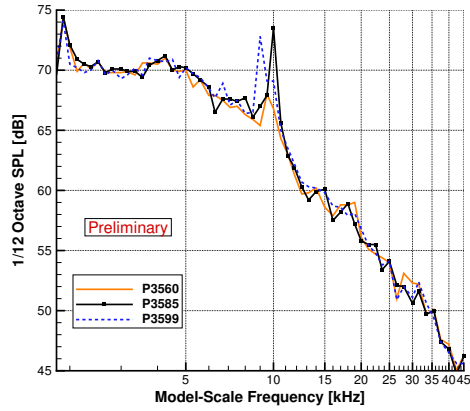
(a) Baseline PSS
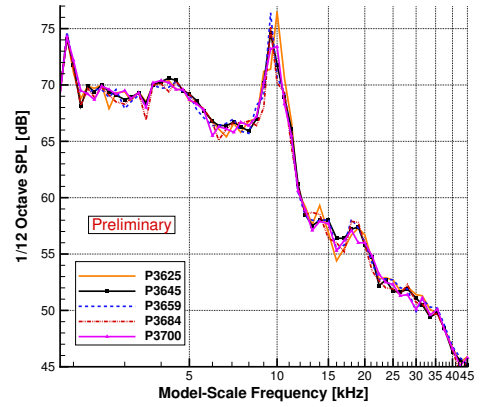
(b) FSS

Fig. 15   Demonstration of data repeatability in processed microphone array spectra from the wing integration region of two HL-CRM configurations tested during the 14x22 experiment at $M = 0.2$ and $\mathbf{AoA} = \mathbf{7.}°$
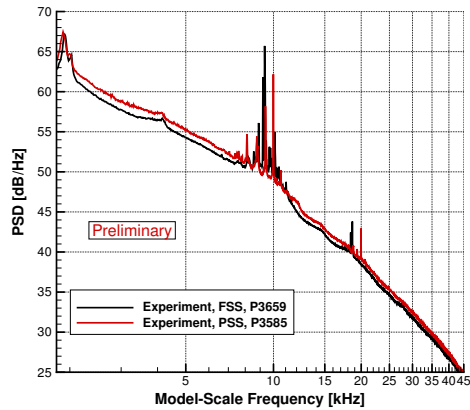
(a) Full spectrum
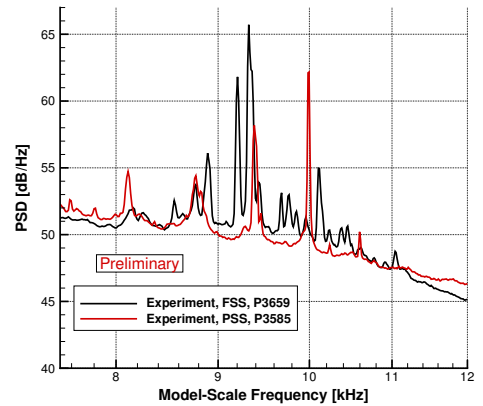
(b) Tones

Fig. 16   14x22 experimental spectra for two HL-CRM configurations. Power spectral density obtained by averaging the spectra of all microphones in the array. $M = 0.2$, $\mathbf{AoA} = \mathbf{7.}°$
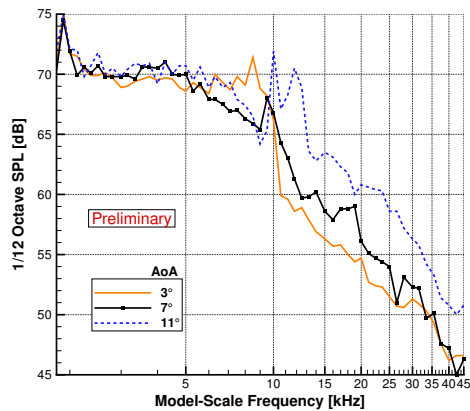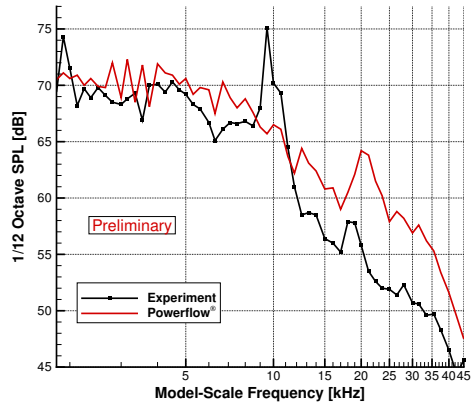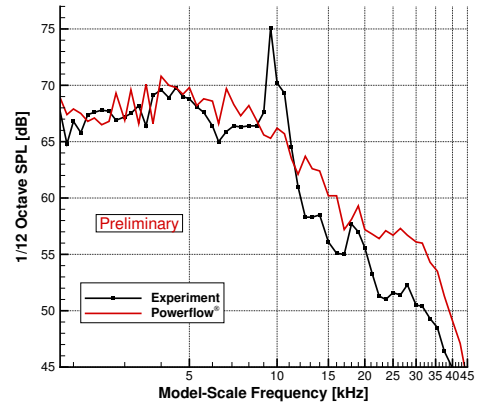

(a) Baseline PSS
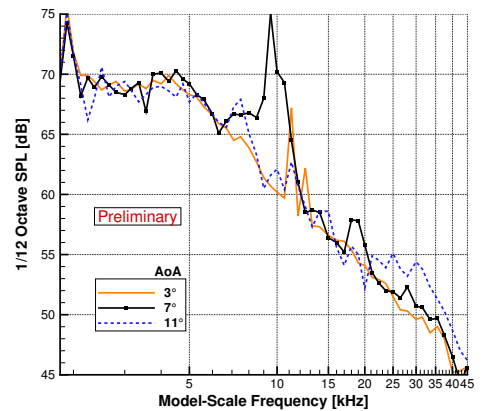
(b) FSS

Fig. 17   14x22 experimental spectra for two HL-CRM configurations demonstrating the effect of the AoA. $M = 0.2$, wing integration region.

(a) Wing

(b) Slat

Fig. 18   Spectra for the FSS HL-CRM configuration at $M = 0.2$. 14x22 experiment at AoA = $7°$ and simulations at AoA = $8°$ in free air. Caption indicates the integration region.

(a) 3 kHz
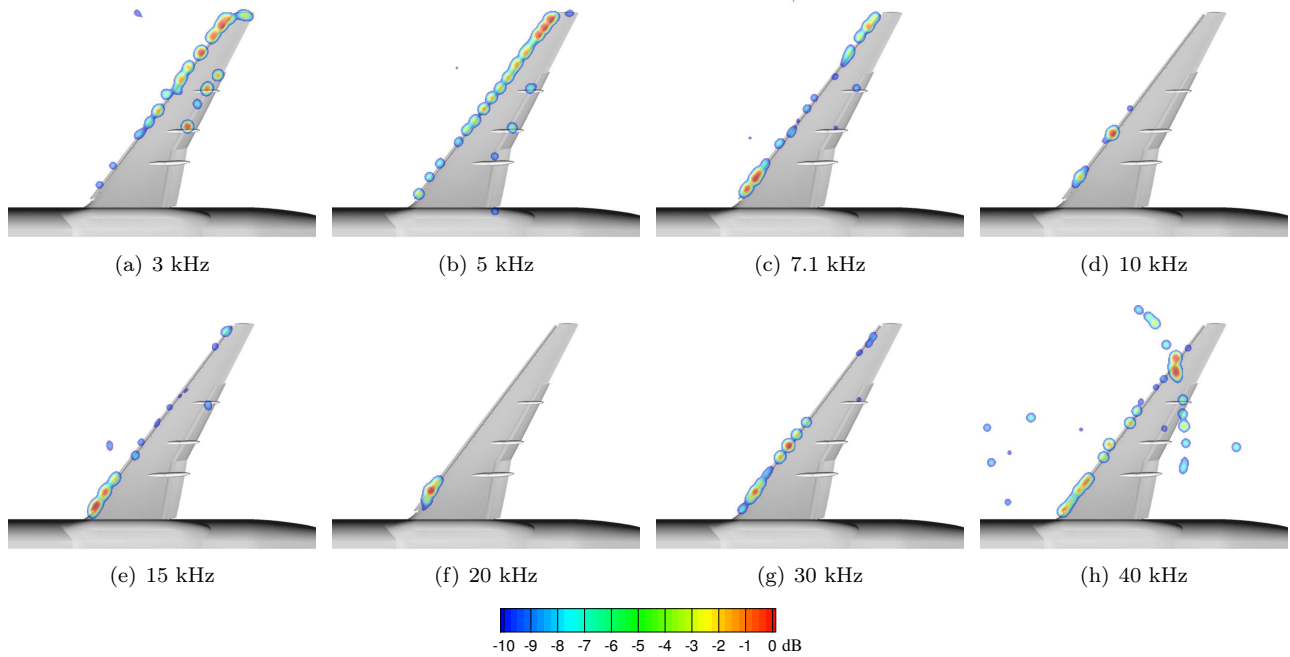
(b) 5 kHz

(c) 7.1 kHz

(d) 10 kHz

(e) 15 kHz

(f) 20 kHz

(g) 30 kHz

(h) 40 kHz

-10 -9 -8 -7 -6 -5 -4 -3 -2 -1 0 dB

Fig. 19   Normalized beamform maps from 14x22 experiment of the FSS HL-CRM configuration. $M = 0.2$ and AoA = $7.°$
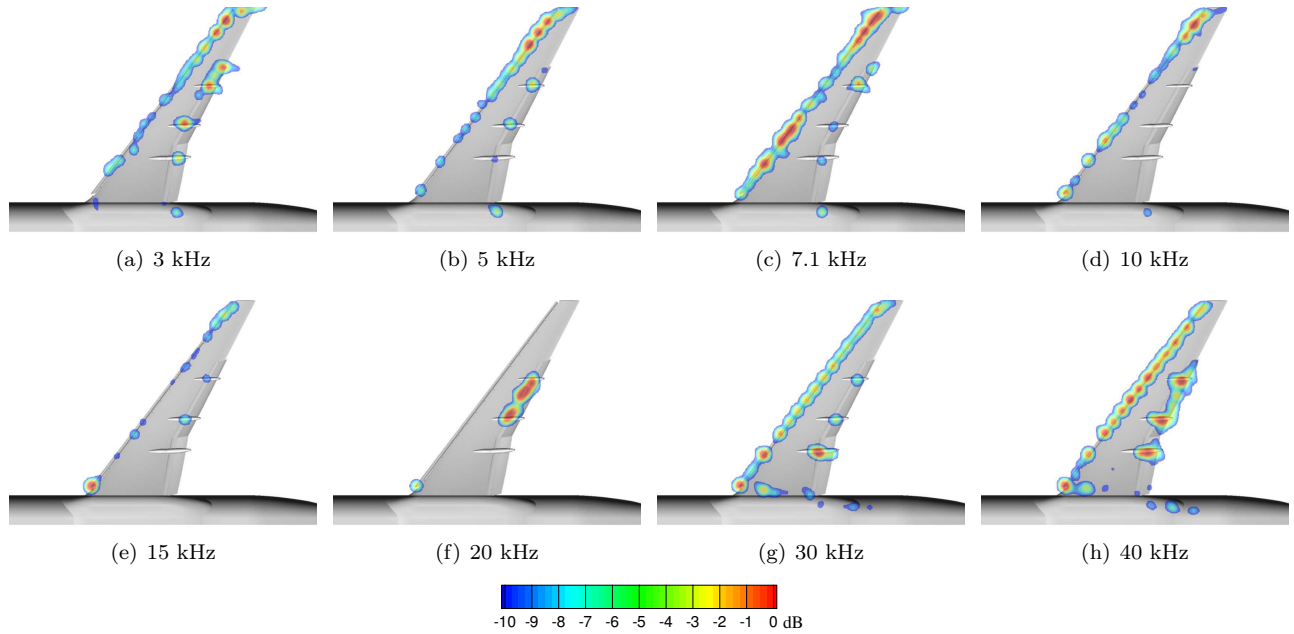
Fig. 20 Beamform maps from PowerFLOW® simulations of the FSS HL-CRM configuration. $M = 0.2$ **and AoA** $= 8°$ **in free air.**
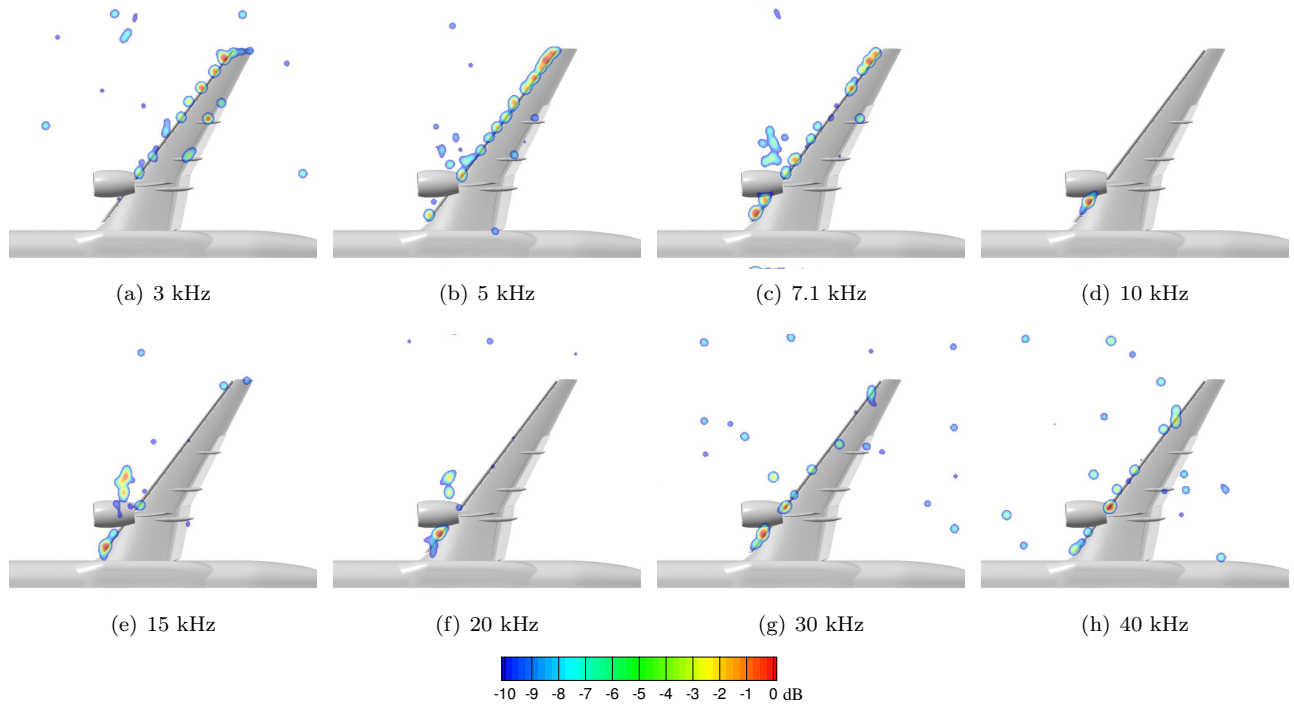

Fig. 21 Beamform maps from 14x22 experiment of the PSS HL-CRM configuration. $M = 0.2$ **and AoA** $= 7°$